



# Li and Si isotopes reveal authigenic clay formation in a palaeo-delta

Xu (Yvon) Zhang, Jérôme Gaillardet, Laurie Barrier, Julien Bouchez

## ► To cite this version:

Xu (Yvon) Zhang, Jérôme Gaillardet, Laurie Barrier, Julien Bouchez. Li and Si isotopes reveal authigenic clay formation in a palaeo-delta. *Earth and Planetary Science Letters*, 2022, 578, pp.117339. 10.1016/j.epsl.2021.117339 . hal-04349544

**HAL Id: hal-04349544**

**<https://hal.science/hal-04349544v1>**

Submitted on 18 Dec 2023

**HAL** is a multi-disciplinary open access archive for the deposit and dissemination of scientific research documents, whether they are published or not. The documents may come from teaching and research institutions in France or abroad, or from public or private research centers.

L'archive ouverte pluridisciplinaire **HAL**, est destinée au dépôt et à la diffusion de documents scientifiques de niveau recherche, publiés ou non, émanant des établissements d'enseignement et de recherche français ou étrangers, des laboratoires publics ou privés.

# Li and Si isotopes reveal authigenic clay formation in a palaeo-delta

Xu (Yvon) Zhang<sup>a, b</sup>, Jérôme Gaillardet<sup>a</sup>, Laurie Barrier<sup>a</sup>, and Julien Bouchez<sup>a</sup>

<sup>a</sup> *Université de Paris, Institut de Physique du Globe de Paris, CNRS, Paris, 75005, France*

<sup>b</sup> *Institut Terre et Environnement de Strasbourg, Université de Strasbourg, CNRS, 5 rue René Descartes, 67084 Strasbourg Cedex, France*

## ABSTRACT

Marine authigenic clay formation has long been postulated as a major process to explain the mass budgets of some elements in seawater, and might act a reverse reaction for the neutralization of atmospheric acidity by soil forming reactions on land. Nevertheless, to date, a handful of studies have directly investigated the effect of reverse weathering due to the challenges associated with sampling complexity. Deltas are thought to be one of the possible environments where reverse weathering reactions may occur because of the abundant influx of weathering derived materials and dynamic activities. In this study, we use a unique combination of three isotope systems (Si, Li, and Nd) as evidence of authigenic clay formation using sediments collected from a ~40 Ma-old delta complex (Ainsa Basin, Spain). Sediments were collected along the land to sea depositional continuum, from alluvial and coastal plains to marine environments. Direct comparison between alluvial, coastal, and marine sediments allows for observing the potential effect of reverse weathering. Systematic differences in Si and Li isotope composition exist between marine and continental sediments, revealing the formation of an authigenic phase sequestering light Li and Si as associated with the diagenesis of Fe in reducing deltaic environments. Finally, this study proposes a geochemical tool for helping distinguishing marine and continental origins of sedimentary rocks when lithofacies and biofacies prove to be ineffective.

## 26    **Key words**

27    Reverse weathering, Li isotopes, Si isotopes, authigenic clays, delta, marine chemistry

## 28    **1. Introduction**

29            The changes in chemical composition of seawater over geological time witness  
30    the co-evolution of input fluxes to the ocean by rivers or seafloor hydrothermal  
31    activities and of output fluxes such as secondary mineral precipitations, *i.e.* as  
32    carbonates or authigenic clay formations (Holland, 2005). The pioneering work of  
33    Mackenzie and Garrels (1966) postulated the existence of so-called “reverse weathering”  
34    processes in the ocean, acting as back reactions of silicate weathering on terrestrial  
35    surfaces (Michalopoulos and Aller, 1995). During reverse weathering in the marine  
36    environment, authigenic clay formation not only takes up cations, but it also consumes  
37    alkalinity, releases CO<sub>2</sub> to the ocean-atmosphere system, modifies the ocean pH,  
38    thereby impacting the geological carbon cycle (*e.g.* Isson et al., 2020; Isson and  
39    Planavsky, 2018; Sillen, 1967). This reverse weathering hypothesis is however  
40    challenging to test as the products of reverse weathering are difficult to identify in  
41    contemporary marine sediments which are overwhelmed by complex mixtures of  
42    terrigenous and biogenic particles. As a consequence, in contrast with silicate  
43    weathering fluxes occurring on terrestrial surfaces, cations fluxes involved in reverse  
44    weathering reactions at the global scale are still poorly known. In addition, it is still  
45    unclear where does reverse weathering occur (coastal margin or in deep-sea sediments)  
46    and how it is affected by different geological settings.

47            Experimental studies using major elements and microscopy techniques have  
48    shown that coastal environments (deltas and estuaries) are viable candidates as sites for  
49    reactions scavenging terrestrially-derived cations through early diagenesis in the

50 sediment column (Michalopoulos and Aller, 2004, 1995). Recently new approaches  
51 using stable and cosmogenic isotopes have identified reverse weathering reactions and  
52 offer the promise to better constrain the fluxes associated with reverse weathering  
53 reactions (*e.g.* Andrews et al., 2020; Bernhardt et al., 2020; Rahman et al., 2016;  
54 Santiago Ramos et al., 2020; Zhang et al., 2021).

55       Among the non-traditional stable isotopes, Li isotopes have proven good  
56 proxies of reverse weathering reactions due to the affinity of Li for secondary minerals  
57 and because the two isotopes of Li,  $^6\text{Li}$  and  $^7\text{Li}$ , are discriminated during their  
58 coprecipitations in clays. Studies conducted in modern estuaries and pore fluids of  
59 marine sediments (Andrews et al., 2020; James and Palmer, 2000; Pogge von  
60 Strandmann et al., 2008) have reported significant isotopic variations. Constraints on  
61 the global Li cycle suggest an outflux of Li from the ocean balancing the influx from  
62 weathering and hydrothermal processes. The uptake of seawater Li by the formation of  
63 authigenic clays during reverse weathering is a strong candidate for such a flux (Li and  
64 West, 2014; Misra and Froelich, 2012). In the critical zone (soil, rivers, groundwaters),  
65 the Li isotope signature appeared to be a powerful tracer for the formation of secondary  
66 minerals in soils or floodplains (*e.g.* Dellinger et al., 2017, 2014; Golla et al., 2021;  
67 Huh et al., 1998), and a good proxy for distinguishing modern products of chemical  
68 weathering (pedogenic) from ancient marine sedimentary rocks (Dellinger et al., 2014).  
69 Reverse weathering processes could enrich Li and shift the isotopic composition of  
70 continental derived solid weathering products toward a  $^7\text{Li}$  enrichment (Teng et al.,  
71 2004). River study in the Amazon and Mackenzie basins have revealed that river  
72 sediments derived from the weathering of a marine sedimentary reservoir clearly appear  
73 to be enriched in Li and isotopically lighter than the modern solid weathering products  
74 derived from granitic rocks (Dellinger et al., 2014). This modification of Li

geochemistry in marine sediments compared to their continental counterparts can occur during early or burial diagenesis processes, and in a variety of environments from estuarine and deltaic zones to the open ocean and within the sedimentary pile.

Although studying modern coastal depositional systems to quantify reverse weathering is the simplest approach to understand early diagenesis processes, it suffers from several issues, chiefly (1) the difficulty of isolating the sediment from seawater or porewater without altering the sediment composition, and (2) limitations encountered when trying to explore the long-term effect of a process studied over relatively short timescales.

Here as an alternative, we turn to a geological analogue to circumvent these difficulties. We investigate the Tertiary Ainsa palaeo-delta system in Spain (Fig. 1), a sedimentological system that has been the object of a breadth of studies aiming at understanding the links between active tectonics and deltaic sedimentary facies and architecture (*e.g.* Caja et al., 2010; Dreyer et al., 1999; Pickering and Bayliss, 2009; Pickering and Corregidor, 2005). This foreland delta was formed during the Eocene, 43 Ma, by the accumulation of erosion products from the then-forming Pyrenees. Refined sequence stratigraphy works have characterized the alluvial, coastal, and marine components from the geometrical and petrological points of view (Dreyer et al., 1999). The advantage of focusing on a palaeo-delta sedimentary series is that it offers a spatially (~1 km) and temporally (~1 Myr) integrated view of the effects of deltaic processes. Although such an approach is associated with potential challenges including sediment preservation and uncertainties about palaeo-seawater chemistry, it allows for probing authigenic effects directly by comparing the marine and continental sediments deposited within a relatively limited time window. To our knowledge, this study is the first investigation of reverse weathering reactions in a palaeo-deltaic system. Our

investigation provides significant evidence for authigenic clay formation in seawater-contacted (marine and coastal) environments.

## **2. Methods**

### **2.1 Field description and sampling strategy**

Samples were collected in the palaeo-deltaic system of the Ainsa Basin (San Vicente, Sobrarbre, and Escanilla formations; Dreyer et al., 1999), which is part of the Southern Pyrenees foreland basin system (Fig. 1A). This well-studied geological object, formed during the Eocene (from middle Lutetian to early Priabonian), is a natural laboratory to compare sedimentary rocks of roughly the same age (albeit deposited within several Myr), mechanically sorted by sediment transport, and deposited along a land-to-sea (hence salinity) continuum. Palaeogeographic reconstructions indicate that the Ainsa Basin developed between the two N-S Mediano and Boltaña anticlines (Fig. 1B). To the south, it is bordered by the Sierras Marginales thrust front. Source material was derived from the then-forming Pyrenees mountain which supplied terrigenous silicates and carbonates to the deltaic system (Caja et al., 2010; Dreyer et al., 1999). Palaeoclimate reconstructions suggest a tropical to subtropical climate with high rainfalls (Pickering and Corregidor, 2005). The relative seawater level varied during basin filling due to local tectonics, as well as glacio-eustatic seawater fluctuations (Dreyer et al., 1999; Pickering and Bayliss, 2009).

Based on a field analysis of the lithology and sedimentary structures, one or several sampling sites were chosen (Fig. 1B and 1C) for each of the main sedimentary environments composing the palaeo-deltaic system of the Ainsa Basin (facies as defined in Bhattacharya, 2006): the alluvial plain (for the upstream alluvial plain and upper delta plain, samples with prefix SA), the coastal plain (for the lower delta plain,

samples with prefix SC), the delta front (samples with prefix SD), and the prodelta (samples with prefix ST). At these sites, deposits with different grain sizes (from micro-conglomerates to claystones) were sampled in order to access the whole spectrum of terrigenous sediments. Examples of sedimentological sections representative of the deposits of the different environments, and of how they were sampled, are shown in Fig. S1. At each site, 4 to 15 unweathered rocks of different grain size were collected, generally along road cuts. During the sampling, the outermost part of each sample was discarded to eliminate any potential effects of present-day weathering. In the field, the colours of the different outcrops were observed to be distinct: alluvial deposits generally exhibit a red colour, typical of oxidized environments, whereas marine deposits show a greyish colour, typical of sediments formed in reducing environments. Detailed information on each sample is listed in Table S1.

## **2.2 Sample preparation, concentrations of major and trace elements in bulk siliciclastic sediments, and isotope measurements**

Thin sections of selected samples were prepared for optical inspection. Then all the collected samples were dried at 50°C and crushed using an agate mortar. Major elements were measured at SARM (Service d'Analyse des Roches et des Minéraux, Vandoeuvre-les-Nancy, France; details of sample preparation analysing methods are provided at <http://helium.crpq.cnrs-nancy.fr/SARM/pages/roches.html>). For trace elements, approximately 0.1 g of the crushed sample powders were dissolved using an HF-HNO<sub>3</sub> method (Dellinger et al., 2014). Trace element concentrations were measured at the Institut de Physique du Globe de Paris (IPGP), using Inductively Coupled Plasma Quadrupole Mass Spectrometry (ICP-Q-MS).

Different powder aliquots were used for measuring Si, Li, and Nd isotopes on Thermo Fisher Neptune Plus MC-ICP-MS (See supplementary materials S1.1-S1.3 for

the methods used for isotope measurements). Sequential extractions of Li pools were performed on selected samples to better constrain the controls on the bulk Li isotope composition of the samples. In the “rinsing” experiments, each sample was rinsed with Milli-Q water (MQ) by repeating the same procedure three times: (1) First, 5 ml MQ water were added to ~1 g sample which was then shaken vigorously for 24 hours; (2) Then, the sample mixture was centrifuged at 4400 rpm and the top 4 ml solution were pipetted out and filtered at 0.2  $\mu\text{m}$ ; (3) Finally, another 4 ml MQ were added into the residual. Additionally, in a separate set of “leaching” experiments, the same previous protocol was applied, but with 0.5 N HCl instead of MQ. The rinsing and leaching solutions were analysed for Li concentration and its isotope composition. We emphasize that the water rinsing and HCl-leaching experiments were carried out on separate aliquots of sediment samples. Therefore, the first HCl leaches likely include solutes that could have been released during the water rinsing experiment. Due to the challenges associated with separate Si between biological and non-biological Si pools and to detection limits of Si measurements, no extraction experiment was conducted for Si.

### **3. Results**

#### **3.1 Texture**

We selected samples from alluvial, coastal, and marine deposits of various grain sizes (from coarse sandstones to fine siltstones) for mineralogical observations on thin sections by optical microscopy. Representative pictures are shown in Fig. S2 and the associated observations are summarized in Table 1. Overall, the thin sections show that source rocks of the sandstones and siltstones deposited in the Ainsa Basin are a mixture of igneous (among which metamorphic) and sedimentary rocks. These deposits are



mainly composed of subangular detrital quartz and carbonates (from crystalline, bioclastic, and micritic limestones), together with minor detrital feldspars, micas, recycled sandstones, and siltstones. In addition, detrital oxides or hydroxides are also common in many samples of the alluvial plain, coastal plain, and prodelta deposits. On the other hand, carbonated bioclasts such as benthic foraminiferas and echinoderm remains are also present in the coarse-grained sediments of the delta front. Between those particles, a calcite cement is visible in the coarse- and medium-grained sandstones of all environments, while a clayey matrix can be observed in the fine-grained sandstones and siltstones. Eventually, micrite can also be observed in the finer-grained samples of the delta front and prodelta deposits.

### **3.2 Major and trace elements**

The major and trace element data are reported in Table S2 and S3, respectively. Grain size exerts a major control on the chemistry of sediments as revealed by the chemical composition of river sediments (*e.g.* Bouchez et al., 2011a). Al/Si ratio can be used as a surrogate for sediment grain size (Bouchez et al., 2011b; Dellinger et al., 2014). The Al/Si ratios of the Ainsa samples range from 0.10 (quartz-rich samples) to 0.44 (clay-rich samples), similar to those observed in modern suspended river sediments (Dellinger et al., 2014). In order to correct the grain size effects (such as the dilution effect of quartz, carbonates, and other potential components in the bulk sample; Dellinger et al., 2014), elemental ratios normalized to Al (X/Al) are reported for major elements (Fig. 2A ranked by increasing X/Al ratios from Mn to Ca) and a number of trace elements (Fig. 2B, ranked by increasing X/Al ratios from Cs to Sr) for different sample groups. Within the variability of each sample groups, major and trace elements do not show significant differences between alluvial, coastal and marine environments. Among major elements, only Fe and Na tend to show slight enrichments in the marine

and coastal sediments compared to their alluvial counterparts. It is also interesting to note that K, which has been shown to be sensitive to reverse weathering or diagenetic reactions (*e.g.* Fedo et al., 1995; Michalopoulos and Aller, 1995; Santiago Ramos et al., 2020), is not enriched in the marine deposits at Ainsa. Regarding trace elements, Li is slightly enriched in marine deposits (Fig. 2B). Finally, it is notable that the Li content of sampled sediments is closely correlated to the combined abundance of Al and Fe therein (Fig. S3).

### 3.3 Li, Si and Nd isotopes and sediment grain size (Al/Si)

$\delta^{30}\text{Si}$ ,  $\delta^7\text{Li}$ , and  $\epsilon\text{Nd}$  were analysed for bulk samples, and their results are reported in Table S1. At Ainsa, grain size displays a strong influence on  $\delta^{30}\text{Si}$  and  $\delta^7\text{Li}$  of sediments, whereas little effect on  $\epsilon\text{Nd}$  (Fig. 3).  $\epsilon\text{Nd}$  values range from -10.0 to -11.9 and are of typical Western Europe upper crustal values (Nägler et al., 1995).  $\delta^{30}\text{Si}$  shows different values among samples ranging from -0.7‰ to -0.1‰. The  $\delta^{30}\text{Si}$  decreases with increasing Al/Si ratio, thus with decreasing grain size, particularly when  $\text{Al/Si} > 0.25$ . The same relationship is observed in river sediments and in shales (Bayon et al., 2018; Savage et al., 2013). The difference in  $\delta^{30}\text{Si}$  among different environments is hardly visible, but seawater-contacted sediments are slightly lighter than the alluvial ones for the higher Al/Si ratios. For example, sediments with  $\delta^{30}\text{Si}$  values lower than -0.4‰ can only be found in coastal and marine environments.

Li isotope compositions show greater variations from -2.4‰ to 6.9‰ and reveal first that  $\delta^7\text{Li}$  is strongly dependent upon grain size as observed in modern-day river sediments (Dellinger et al., 2014), and second that the different sample groups show significant differences in  $\delta^7\text{Li}$  with marine sediments having lower  $\delta^7\text{Li}$  values ( $\delta^7\text{Li}=1.0 \pm 4.4\text{‰}$ ,  $2\sigma$ ) than alluvial ones ( $\delta^7\text{Li}=3.9 \pm 3.4\text{‰}$ ,  $2\sigma$ ). The coastal plain

samples lie in between ( $\delta^7\text{Li}=2.6 \pm 3.8\text{‰}$ ,  $2\sigma$ ). The negative relationship between  $\delta^7\text{Li}$  and Al/Si in alluvial sediments is similar (although shifted toward higher values) to what is observed in modern-day river sediments (Dellinger et al., 2014).

An enrichment of Li in marine sediments accompanied by a fractionation which favours light Li in these sediments is observed when we compare the  $\delta^7\text{Li}$  and Li/Al ratio among different deposits (Fig. 4). The probability densities of Li/Al and  $\delta^7\text{Li}$  were estimated using Kernel Density Estimations with programs provided by Pedregosa et al., (2011) and are respectively displayed in Fig. 4. A slight enrichment of Li in the marine sediments can be observed: marine samples have higher Li/Al ( $\text{Li/Al}=1.17\pm0.27\times10^{-3}$ ) values compared to alluvial samples ( $\text{Li/Al}=1.05\pm0.26\times10^{-3}$ ).

The different sediment groups display significantly different  $\delta^7\text{Li}$  fingerprints with marine sediments have lighter  $\delta^7\text{Li}$  signatures than alluvial sediments. This is first shown by statistical analysis with  $p<0.05$  (t-test, two tails) between any two environments and is visually displayed by a gradual decrease of  $\delta^7\text{Li}$  values corresponding to the peaks of probability densities from alluvial to marine phase sediments. Namely the probability densities are maximal at  $\delta^7\text{Li}$  equals to 2.9 ‰ for alluvial sediments, 1.9 ‰ for costal sediments, and 0.4 ‰ for marine sediments. The difference of  $\delta^7\text{Li}$  between marine and alluvial sediments is approximately -3 ‰.

### 3.4 Sequential extractions of Li pools

Initially, two Li pools (palaeo-seawater and carbonate) from the sediment samples were targeted and expected to be extracted. To access these pools, we have opted for a simple and convenient extraction method, which can provide first-order understanding of the Li pools presenting in the palaeo-delta sediments. We note here that any leachate should rather be envisaged as operationally defined as no chemical

extraction protocol is perfect.

The first Li pool was extracted from rinsing the sample powder with MQ. This water-rinseable Li pool represents the loosely-bound and possibly surface layer sites Li fractions, presumably containing Li from seawater inclusion and adsorbed Li during clay-seawater interaction in clay minerals (*e.g.* Zhang et al., 2021). Overall, as shown in Table 2, 0.32-0.87% of total Li was rinsed from seawater-contacted samples (marine and coastal), whereas this “rinseable” fraction of Li was 0.17-0.43% in alluvial samples. A first-order observation is thus that the seawater-contacted samples contain more rinseable Li compared to alluvial sediments. This small difference in the rinseable Li fraction between seawater-contacted and alluvial sediments may be attributed to a small seawater influence on the sediments. Except for the alluvial samples that have a too-low amount of rinseable Li, the isotope signature of this rinsed fraction was measured for marine sediments and whose values range from 1.91‰ to 12.84‰.

The second Li pool was expected to be Li contained in carbonates. Unlike the water-rinsing experiment, significant amounts of cations were extracted during the HCl-leaching experiments (Fig. S4). In these leachates, the dissolved substances can correspond to cations released from the exchangeable sites (also leached to some extent by MQ), carbonates, oxides, clays, and probably primary minerals. Our approach was thus to use a stepwise HCl leaching procedure, in order to roughly separate the Li from all those pools. In all samples, Ca, which is indicative of carbonates, was significantly extracted during the 3 steps of the leaching procedure, in a consistently decreasing fashion, such that at the end of the leaching experiment, a significant fraction of bulk Ca had been extracted for all samples (~55% to ~100% of total Ca, Fig. S4 and Table S4). In the samples where Ca was significantly extracted (>90%), other metals such as Li, Al, or Fe started to be extracted in the second or third step of the procedure as

indicated by the Al/Ca and Fe/Ca ratios, which can be quantitatively indicative of different Li pools (Bastian et al., 2018), in the successive leachates (Table 3). Generally, in the first leachates, the Al/Ca and Fe/Ca ratios are low ( $\sim 10^{-6}$ - $10^{-5}$ ) indicating that Li in the first leachates is sourced from a rinseable Li pool and from a carbonate Li pool. In the last leachates, the Al/Ca and Fe/Ca become significantly higher ( $\sim 10^{-2}$ - $10^{-1}$ ), suggesting that carbonate was dissolved during the previous leaching steps, and that the Li in the last leachates is sourced from the Al-Fe-associated Li pool.

Only the  $\delta^7\text{Li}$  compositions of the first (rinseable Li and carbonate-bound Li) and third (Al-Fe-associated Li) leachate solutions were measured (Table 3). The  $\delta^7\text{Li}$  compositions in the first leachates were characterized by values close to or heavier than the bulk  $\delta^7\text{Li}$ , whereas the  $\delta^7\text{Li}$  of the last leachates were characterized by values lighter than the bulk  $\delta^7\text{Li}$  (Fig. S5). The leaching results of sample SD7 seem to be opposite to observations from other samples, which we attribute to the low carbonate content in this sample. In sample SD7, the Al-Fe-associated Li was most likely released “earlier” (*i.e.* during the first leaching step) than in other samples, resulting in a Li isotope composition consistent with what is expected for the Al-Fe-associated Li pool.

Among these different Li pools, rinseable and carbonate Li have a minor effect ( $<1.5\%$  of total Li, Fig. S4) on the  $\delta^7\text{Li}$  signatures of Ainsa sediments but the Al-Fe-associated Li plays an important role on the bulk Li signature: sequential extractions show that a significant portion (4% to 42% of bulk Li, Fig. S4) of light Li ( $\delta^7\text{Li}=-6.0\text{‰}$  to  $-2.8\text{‰}$ ) is present as an (Al-Fe)-associated Li pool in seawater-contacted (marine and coastal) sediments, whereas this portion of Li is relatively smaller (5% to 16% of bulk Li) and heavier ( $\delta^7\text{Li}=-2.3\text{‰}$  to  $0.1\text{‰}$ ) in alluvial sediments. Although the enrichment of  $^6\text{Li}$  in the Al-Fe component is observed for both seawater-contacted and alluvial sediments, the  $\delta^7\text{Li}$  difference between this Li pool and bulk Li is generally

greater in the marine deposits than in the alluvial ones (Fig. S5).

## **4. Discussion**

Overall, our results show that Li (and to a lesser extent Si) isotopes are very sensitive proxies distinguishing between marine and continental depositional environments – much more than concentrations of Li or other major/trace elements. River studies have shown that one major cause of  $\delta^7\text{Li}$  and  $\delta^{30}\text{Si}$  variability in modern-day river sediments is grain size (Bayon et al., 2018; Dellinger et al., 2014). In this study, grain size effects were taken into account by comparing the isotopic signature of different sedimentary bodies as a function of Al/Si. As indicated by Fig. 3, isotopic shifts between alluvial and marine samples occur for all range of Al/Si values and are therefore not due to changes in grain size. In the following, we thus discuss the possible causes for the isotopic variabilities in Si and Li that characterize the Ainsa palaeo-delta sediments.

### **4.1 Ruling out the effect of temporal variations of rock source material and weathering regime**

As pointed out above, the Ainsa palaeo-delta was formed within a couple of million years. Because it was impossible to sample rocks of exactly the same age in the field, a possible explanation of the variations in  $\delta^7\text{Li}$  and  $\delta^{30}\text{Si}$  of the different sedimentary units could be temporal changes in the parent material or in the weathering processes in the upstream watersheds.

As shown by a large number of studies, continental silicate rocks are rather homogeneous in terms of  $\delta^7\text{Li}$  and  $\delta^{30}\text{Si}$ , with the exception of shales, which are enriched in Li and have lower  $\delta^7\text{Li}$  and  $\delta^{30}\text{Si}$  than granitic rocks (Dellinger et al., 2014; Savage et al., 2013). If the Li isotopic variations reported in this study were essentially

due to mixing between different rock sources, Fig. 4 should be seen as a mixing diagram between at least three end-members whose contribution changed with time. The continental samples define a potential mixing line between a granitic end-member and a shale end-member, close (but not exactly same) to what Dellinger et al. (2014) found in the modern sediments transported by the Amazon and Mackenzie rivers ( $\delta^7\text{Li} = 5 \pm 1\text{‰}$ ,  $\text{Li}/\text{Al} = 0.5 \pm 0.1 \times 10^{-3}$  for the granitic end-member and  $\delta^7\text{Li} = 1 \pm 1\text{‰}$ ,  $\text{Li}/\text{Al} = 1 \pm 0.1 \times 10^{-3}$  for the shale end-member). However, the marine and coastal samples would necessitate a third endmember, enriched in Li and more depleted in  $^7\text{Li}$ , to be explained (Fig. 4). Such an end-member has not been found in modern-day weathering products. The fact that palaeogeographic reconstructions indicate no changes of provenance during the construction of the Ainsa delta (Caja et al., 2010; Dreyer et al., 1999), and that the Nd isotopes (not fractionated by weathering processes, McLennan, 1989) show invariant  $\epsilon\text{Nd}$  values (Fig. 3), also suggest a negligible variation of source rocks of all samples measured in this study, which does not support the idea that the Li and Si isotopic variability can be explained by a mixture of different parent materials changing through time.

Alternatively, the observed isotopic changes between the different sediment formations of the Ainsa palaeo-delta could be due to temporal variations in weathering regimes within the sampled time window. We know from modern river systems that Li isotope ratios of secondary solid products of chemical weathering vary as a function of the weathering regime (Dellinger et al., 2017). Intensive weathering, *i.e.* high  $W/(W+E)$  ratio (where  $W$  is the chemical erosion flux and  $E$  the physical erosion, Bouchez and Gaillardet, 2014), results in lower river sediment  $\delta^7\text{Li}$ . Using this principle, the difference in  $\delta^7\text{Li}$  between marine and alluvial sediments could be interpreted as resulting from different weathering regimes on the continent: a higher weathering

intensity reflected in the marine sediments compared to the alluvial ones. This scenario would however imply a stronger Li-depletion in marine sediments, *i.e.* a stronger solubilization of Li which produces lower Li/Al ratios in the solids (Dellinger et al., 2014). We observe the opposite in Ainsa sediments (Fig. 4). Therefore, the observed isotopic shifts between marine and alluvial sediments in Ainsa are unlikely to be related to changes in provenance or weathering regime with time, but rather to processes that operated in the palaeo-delta such as the scavenging of dissolved Li into sediments through authigenic mineral formations.

#### **4.2 Evidence for the presence of an authigenic phase incorporating light Li and Si.**

We can interpret Fig. 4 as reflecting the existence of an authigenic component contained in the marine sediments (and coastal sediments to a lesser extent), enriched in Li (high Li/Al) and with  $\delta^7\text{Li}$  lower than -3‰. Such a low value agrees with that found in the leached phase in the HCl experiments.

The MQ rinsing experiments and the sequential extraction experiments using HCl show that the only significant pool of extractable Li is associated with Al and Fe, thus probably to Fe-bearing clay minerals, and that this Li pool displays a low  $\delta^7\text{Li}$ . The absence of this Li fraction in the MQ rinsing solution suggests that this extractable Li pool does not correspond to Li adsorbed or Li hosted in seawater inclusions. It is important to note that all sediments groups from alluvial plains, coastal, and marine environments show this extractable Li component even if it appears to be more important in the seawater-contacted sediments. We interpret these results as indicating the presence of an authigenic phase characterized by high contents of Al and Fe, mostly present in the marine sediments of the Ainsa palaeo-delta. We emphasize that this Li pool is a key to interrogate reverse weathering processes and it was often overlooked in previous studies based on Li isotopes in sedimentary records (*e.g.* Yang et al., 2021).



370 From an isotopic point of view, it is now well admitted that the incorporation of  
371 Li in secondary phases at low temperature favours the light Li isotope (*e.g.* Andrews et  
372 al., 2020; Hindshaw et al., 2019; Vigier et al., 2008; Zhang et al., 2021). Leached  
373 solutions from Ainsa sediments are enriched in  $^6\text{Li}$ , and are therefore consistent with  
374 the presence of an authigenic component. Authigenic clay formation has been  
375 suggested to take place in the water column of an Icelandic estuary by Pogge von  
376 Strandmann et al., (2008). In this study, the authors interpreted the  $\delta^7\text{Li}$  of suspended  
377 sediments as indicating the addition to basalt-derived detrital material of an authigenic  
378 component having a  $\delta^7\text{Li}$  19‰ lower than seawater, consistent to the fractionation  
379 factor ( $\sim -20\text{‰}$ ) obtained from experimental studies (*e.g.* Zhang et al., 2021). Based on  
380 the available seawater  $\delta^7\text{Li}$  reconstructions, Eocene seawater  $\delta^7\text{Li}$  should be close to  
381  $\sim 24\text{‰}$  (Misra and Froelich, 2012) and thus inferred  $\delta^7\text{Li}$  value of the Ainsa authigenic  
382 component should be close to 4-5‰ assuming the same apparent fractionation factor.  
383 This value is higher than the inferred authigenic component in this study ( $< -3\text{‰}$ ),  
384 suggesting that the authigenic phase in Ainsa may not have precipitated directly from  
385 Eocene seawater. To explain the  $< -3\text{‰}$   $\delta^7\text{Li}$  signature inferred from Fig. 4, applying a  
386 Li isotope fractionation factor of  $\sim -20\text{‰}$ , the source of Li to authigenic phases should  
387 have a  $\delta^7\text{Li}$  signature lower than 17‰. A viable candidate for such a signature would  
388 be the sediment porewater. Although it is impossible to know the local  $\delta^7\text{Li}$  of the  
389 porewater when Ainsa sedimentary rocks formed, we note that the modern pore water  
390 recovered from coastal environments typically has  $\delta^7\text{Li}$  values lower than that of  
391 seawater (James and Palmer, 2000).

392 The effect of reverse weathering on oceanic Si isotope composition has been  
393 long speculated (Frings et al., 2016 and references therein), and yet only limited  
394 information is available from a handful of previous studies, which in particular showed

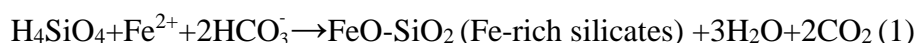
that authigenic clay formation is linked to the diagenesis of biogenic Si (BSi; *e.g.* Ehlert et al., 2016; Geilert et al., 2020; Michalopoulos and Aller, 2004; Rahman et al., 2017, 2016). The Si isotope signature of the BSi source at Ainsa is unknown, which in conjunction with the lack of constraints on Si isotope fractionation during BSi diagenesis, hampers interpretation of our results beyond a first-order glimpse on the potential role of authigenic clay formation on Si isotopes. However, the slight difference in  $\delta^{30}\text{Si}$  between the alluvial and seawater-contacted samples suggests that the newly formed authigenic phase preferentially takes up light Si, in agreement with previous findings from the precipitation of Si-bearing phases (*e.g.* Ehlert et al., 2016; Geilert et al., 2020; Oelze et al., 2015).

Importantly, the lower  $\delta^{30}\text{Si}$  signature of seawater-contacted sediments is observed for samples with a high Al/Si ratio. In the context of previous studies on river sediments (*e.g.* Bouchez et al., 2011), this can be interpreted as the fine end-member of detrital sediment grain size undergoing the largest extent of authigenic clay formation, provided that this latter reaction does not shift significantly the sediment Al/Si ratio towards lower values through the incorporation of BSi. We argue that the Al/Si ratio is relatively stable during these reactions. First, Al is an immobile element and the source of Al for authigenic clay formation is thought to be the alteration of terrigenous Al-oxides and aluminosilicates (Michalopoulos and Aller, 1995). Therefore, the bulk Al content should be the same between continental and marine sediments. Regarding Si, although we are still lacking detailed information on authigenic clay formation, this Si flux to the sediment due to reverse weathering process is considered to be relatively small (Frings et al., 2016) when compared to detrital Si content delivery to the oceans (Milliman and Farnsworth, 2013). As both bulk sediment Al and Si concentrations are not significantly modified by authigenic clay formation, the Al/Si ratio remains

relatively unchanged during diagenesis. As a consequence, the lower  $\delta^{30}\text{Si}$  in high-Al/Si marine sediments is indeed evidence for finer detrital fractions being more prone to authigenic clay formation.

### **4.3 A possible reverse weathering pathway coupling Fe cycle in marine environment**

In the Ainsa palaeo-delta, the presence of authigenic clays is suggested by the enrichment of light Li isotopes in seawater-contacted sediments. Moreover, the Li isotope geochemistry is closely linked to Fe cycling in marine environments. First, as indicated by Fig. 5, in bulk samples correlations exist between  $\delta^7\text{Li}$  and Li/Fe or Li/(Fe+Al), particularly for marine sediments. Second, the leaching experiment shows that light Li isotopes, which is indicative of the authigenic clays, is associated with an Al-Fe phase (Figs. S4 and S5). It is important to note that the range of isotopic values found in this Al-Fe-associated Li pool is compatible with that inferred ( $< -3\text{‰}$ ) from the mixing diagram of Figs. 3 and 4. Beyond our study in Ainsa, the association between  $\delta^7\text{Li}$  and Fe content was also found in other marine sedimentary rocks (Qiu et al., 2009). Therefore, our study provides evidence that reverse weathering, in certain geological context such as deltas, is coupled with the marine Fe cycle. Indeed, river deltas are known to act as a major sink of riverine dissolved Fe through colloidal flocculation and particle adsorption (*e.g.* Sholkovitz, 1976). The rapid formation of Fe-bearing products could then lead to efficient light Li sorption in the water column (Pistiner and Henderson, 2003). Once deposited in the sediment column, early diagenesis in reducing marine environments would then allow for the formation of  $\text{Fe}^{2+}$ -rich phases, such as oxides and Fe-rich aluminosilicates. Such processes can be possibly achieved by following reaction:



The Fe-rich silicates minerals could incorporate Li, as  $\text{Li}^+$  and  $\text{Fe}^{2+}$  share similar ionic radii (Shannon, 1976). Iron-rich compositions are a common feature of authigenic minerals such as greenalite and odinite (*e.g.* Isson and Planavsky, 2018), which form relatively rapidly in the sediment column (Michalopoulos and Aller, 2004, 1995). This Fe-rich phase is likely driven by the co-precipitation of Fe and Si (*e.g.* Wu et al., 2012). The association of Li with an Al–Fe pool in Ainsa sediments can therefore be interpreted as the formation of authigenic clays in a reducing environment in the delta, for example in the sedimentary column.

A recent study of the authigenic formation effect on Li geochemistry in a carbonate-rich unit from deep-sea environment (Andrews et al., 2020) suggests that significant clay neoformation occurs in the sedimentary column at depth further away from the seawater-sediment interface. In contrast to results from an estuary in Iceland (Pogge von Strandmann et al., 2008) and experimental constraints on authigenic formation (Zhang et al., 2021), where rapid early diagenesis predominate, slow burial diagenesis controls the uptake of Li into authigenic phase at geological time scales. Although our limited dataset does not permit us to fully explore the roles of both early and burial diagenesis, we speculate that our results are driven by early diagenesis processes as the authigenic phase is closely coupled to rapid Fe cycle (*e.g.* Sholkovitz, 1976) and the deltaic environments, where detrital materials are abundant and these materials can be further dissolved during the interaction with seawater, allows for early diagenesis processes (*e.g.* Michalopoulos and Aller, 1995). Furthermore, the  $\delta^7\text{Li}$  fingerprint used in this study to trace authigenic formation shows a gradual decrease along the land-to-sea continuum, and the authigenic phase is not only observed in marine sediments but also in coastal settings where the burial effect is minor. This suggests the authigenic processes occurred in the Ainsa delta was rather impacted by

early diagenesis effects.

At the Ainsa palaeo-delta, we observe that these reactions tied to Fe act as a sink for Li into the sediments and causes a fractionation resulting in a heavier  $\delta^7\text{Li}$  in water. This deltaic process identified in this study therefore contributes to enrich marine shales in Li (Dellinger et al., 2014) even if the Li/Al difference between marine and non-marine material is tight (Fig. 4). The contradictory observation between Ainsa marine sediments where light Li is preferred and shales having heavy  $\delta^7\text{Li}$  values (Teng et al., 2004) indicates other mechanisms enriching Li in marine sedimentary rocks, such as the precipitation of other Li-bearing phases in other geological contexts or more probably during burial diagenesis (Andrews et al., 2020). The enrichment of Na in the seawater-contacted sediments observed at Ainsa compared to alluvial sediments (Fig. 5) is noteworthy. As the Na abundance of the HCl-leach extracts is similar among different environments, the enrichment of Na in the coastal and marine sediments can be attributed to its incorporation into authigenic phases (*e.g.* phyllosilicates), rather than to seawater inclusions. Nevertheless, the enrichment of the heavy alkali elements K, Rb, and Cs is less significant in the case of Ainsa (Table S5). Although K has been shown to be taken up by reverse weathering reactions (*e.g.* Michalopoulos and Aller, 1995), our results suggest the diagenetic phases that formed in the Ainsa delta do not play a major role of seawater K sequestration. This difference in terms of K uptake between a palaeo-delta archive (this study) and modern delta systems (Michalopoulos and Aller, 1995) requires further work to understand the mechanism controlling K sinks in the ocean (Holland, 2005).

## 5. Conclusion

The fact that at Ainsa, the Si and Li isotope compositions in marine and coastal

494 plain sediments are lighter than in alluvial ones, together with the associated enrichment  
495 in the soluble cation Li and Na, suggest that formation of Fe-rich authigenic clays in  
496 deltaic environments is an important process for ocean elemental and isotope budgets.

497 Our results show that light Li is incorporated into seawater-contacted sediments,  
498 particularly the marine sediments in deltaic environments, resulting in a lower  $\delta^7\text{Li}$   
499 signature than in alluvial ones. This observation is in contrast to that made on ancient,  
500 fine-grained marine sedimentary rocks (Dellinger et al., 2014; Teng et al., 2004).  
501 Similar to continental weathering processes which can not be ascribed to a single  
502 reaction, reverse weathering reactions are likely associated with complex diagenesis  
503 processes and different yet-unidentified reactions, and here we have one which couples  
504 Li, Si, and Fe cycles in the deltas.

505 Furthermore, our study supports a strong coupling among Fe, Li, and Si in deltaic  
506 environments (coastal and marine) through the neoformation of authigenic  
507 phyllosilicates in reducing conditions. This process is typical of a reverse weathering  
508 reaction as proposed initially, in that it consumes alkalinity and produces  $\text{CO}_2$  in the  
509 atmosphere-ocean system (Isson et al., 2020; Mackenzie and Garrels, 1966; Sillen,  
510 1967). By consuming ocean alkalinity, it acts as a counterbalancing reaction to the  
511 neutralization of atmospheric  $\text{CO}_2$  through silicate weathering reactions transforming  
512 rocks into soils in the terrestrial Critical Zone. Finally, our investigation clearly  
513 demonstrates that reverse weathering reactions existed at the time of deposition, and Li  
514 isotopes can be useful to constrain the marine or continental origin of sedimentary rocks.  
515 Such a tool is important in paleo-environmental studies including reconstruction of past  
516 living environments or the formation of mountain ranges when arguments based on  
517 sedimentary facies or fossil organisms are not conclusive.

518

519    **Acknowledgements**

520    We sincerely thank those helped in this project, particularly Amandine Laborde for  
521    sampling assistance in the field, Marc Quintin for thin section preparation, and Laëticia  
522    Faure for Nd isotope analysis. This research is fully funded by the People Programme  
523    (Marie Curie Actions) of the European Union's Seventh Framework Programme  
524    FP7/2007-2013/ under REA grant agreement [608069, ISONOSE]. Part of this work  
525    was supported by the IPGP multidisciplinary program PARI and the Region île-de-  
526    France SESAME Grant no. 12015908.

527 **References:**

- 528 Andrews, E., Pogge von Strandmann, P.A.E., Fantle, M.S., 2020. Exploring the  
529 importance of authigenic clay formation in the global Li cycle. *Geochim.*  
530 *Cosmochim. Acta* 289, 47–68. <https://doi.org/10.1016/j.gca.2020.08.018>
- 531 Bastian, L., Vigier, N., Reynaud, S., Kerros, M.-E., Revel, M., Bayon, G., 2018.  
532 Lithium Isotope Composition of Marine Biogenic Carbonates and Related  
533 Reference Materials. *Geostand. Geoanalytical Res.* 42, 403–415.  
534 <https://doi.org/10.1111/ggr.12218>
- 535 Bayon, G., Delvigne, C., Ponzevera, E., Borges, A. V, Darchambeau, F., De Deckker,  
536 P., Lambert, T., Monin, L., Toucanne, S., André, L., 2018. The silicon isotopic  
537 composition of fine-grained river sediments and its relation to climate and  
538 lithology. *Geochim. Cosmochim. Acta* 229, 147–161.
- 539 Bernhardt, A., Oelze, M., Bouchez, J., von Blanckenburg, F., Mohtadi, M., Christl, M.,  
540 Wittmann, H., 2020.  $^{10}\text{Be}/^{9}\text{Be}$  ratios reveal marine authigenic clay formation.  
541 *Geophys. Res. Lett.* 47, e2019GL086061. <https://doi.org/10.1029/2019GL086061>
- 542 Bhattacharya, J.P.P., 2006. Deltas, Facies Models Revisited. SEPM Society for  
543 Sedimentary Geology. <https://doi.org/10.2110/pec.06.84.0237>
- 544 Bouchez, J., Gaillardet, J., 2014. How accurate are rivers as gauges of chemical  
545 denudation of the Earth surface? *Geology* 42, 171–174.
- 546 Bouchez, J., Lupker, M., Gaillardet, J., France-Lanord, C., Maurice, L., 2011a. How  
547 important is it to integrate riverine suspended sediment chemical composition with  
548 depth? Clues from Amazon River depth-profiles. *Geochim. Cosmochim. Acta* 75,  
549 6955–6970. <https://doi.org/https://doi.org/10.1016/j.gca.2011.08.038>
- 550 Bouchez, J., Métivier, F., Lupker, M., Maurice, L., Perez, M., Gaillardet, J., France-  
551 Lanord, C., 2011b. Prediction of depth-integrated fluxes of suspended sediment in



552 the Amazon River: particle aggregation as a complicating factor. *Hydrol. Process.*  
 553 25, 778–794. <https://doi.org/10.1002/hyp.7868>  
 554 Caja, M.A., Marfil, R., Garcia, D., Remacha, E., Morad, S., Mansurbeg, H., Amorosi,  
 555 A., Martínez-Calvo, C., Lahoz-Beltrá, R., 2010. Provenance of siliciclastic and  
 556 hybrid turbiditic arenites of the Eocene Hecho Group, Spanish Pyrenees:  
 557 implications for the tectonic evolution of a foreland basin. *Basin Res.* 22, 157–180.  
 558 <https://doi.org/10.1111/j.1365-2117.2009.00405.x>  
 559 Dellinger, M., Bouchez, J., Gaillardet, J., Faure, L., Moureau, J., 2017. Tracing  
 560 weathering regimes using the lithium isotope composition of detrital sediments.  
 561 *Geology* 45, 411–414.  
 562 Dellinger, M., Gaillardet, J., Bouchez, J., Calmels, D., Galy, V., Hilton, R.G., Louvat,  
 563 P., France-Lanord, C., 2014. Lithium isotopes in large rivers reveal the  
 564 cannibalistic nature of modern continental weathering and erosion. *Earth Planet.*  
 565 *Sci. Lett.* 401, 359–372.  
 566 <https://doi.org/http://dx.doi.org/10.1016/j.epsl.2014.05.061>  
 567 Dreyer, T., Corregidor, J., Arbues, P., Puigdefabregas, C., 1999. Architecture of the  
 568 tectonically influenced Sobrarbe deltaic complex in the Ainsa Basin, northern  
 569 Spain. *Sediment. Geol.* 127, 127–169.  
 570 Ehlert, C., Doering, K., Wallmann, K., Scholz, F., Sommer, S., Grasse, P., Geilert, S.,  
 571 Frank, M., 2016. Stable silicon isotope signatures of marine pore waters –  
 572 Biogenic opal dissolution versus authigenic clay mineral formation. *Geochim.*  
 573 *Cosmochim. Acta* 191, 102–117.  
 574 <https://doi.org/https://doi.org/10.1016/j.gca.2016.07.022>  
 575 Fedo, C.M., Wayne Nesbitt, H., Young, G.M., 1995. Unraveling the effects of  
 576 potassium metasomatism in sedimentary rocks and paleosols, with implications

577 for paleoweathering conditions and provenance. *Geology* 23, 921–924.  
578 [https://doi.org/10.1130/0091-7613\(1995\)023<0921:UTEOPM>2.3.CO;2](https://doi.org/10.1130/0091-7613(1995)023<0921:UTEOPM>2.3.CO;2)

579 Frings, P.J., Clymans, W., Fontorbe, G., De La Rocha, C.L., Conley, D.J., 2016. The  
580 continental Si cycle and its impact on the ocean Si isotope budget. *Chem. Geol.*  
581 425, 12–36. <https://doi.org/http://dx.doi.org/10.1016/j.chemgeo.2016.01.020>

582 Geilert, S., Grasse, P., Doering, K., Wallmann, K., Ehlert, C., Scholz, F., Frank, M.,  
583 Schmidt, M., Hensen, C., 2020. Impact of ambient conditions on the Si isotope  
584 fractionation in marine pore fluids during early diagenesis. *Biogeosciences* 17,  
585 1745–1763. <https://doi.org/10.5194/bg-17-1745-2020>

586 Golla, J.K., Kuessner, M.L., Henehan, M.J., Bouchez, J., Rempe, D.M., Druhan, J.L.,  
587 2021. The evolution of lithium isotope signatures in fluids draining actively  
588 weathering hillslopes. *Earth Planet. Sci. Lett.* 567, 116988.  
589 <https://doi.org/https://doi.org/10.1016/j.epsl.2021.116988>

590 Hindshaw, R.S., Tosca, R., Goût, T.L., Farnan, I., Tosca, N.J., Tipper, E.T., 2019.  
591 Experimental constraints on Li isotope fractionation during clay formation.  
592 *Geochim. Cosmochim. Acta* 250, 219–237.

593 Holland, H.D., 2005. Sea level, sediments and the composition of seawater. *Am. J. Sci.*  
594 305, 220–239.

595 Huh, Y., Chan, L.-H., Zhang, L., Edmond, J.M., 1998. Lithium and its isotopes in major  
596 world rivers: implications for weathering and the oceanic budget. *Geochim.*  
597 *Cosmochim. Acta* 62, 2039–2051. [https://doi.org/https://doi.org/10.1016/S0016-](https://doi.org/https://doi.org/10.1016/S0016-7037(98)00126-4)  
598 [7037\(98\)00126-4](https://doi.org/https://doi.org/10.1016/S0016-7037(98)00126-4)

599 Isson, T.T., Planavsky, N.J., 2018. Reverse weathering as a long-term stabilizer of  
600 marine pH and planetary climate. *Nature* 560, 471.

601 Isson, T.T., Planavsky, N.J., Coogan, L.A., Stewart, E.M., Ague, J.J., Bolton, E.W.,

602 Zhang, S., McKenzie, N.R., Kump, L.R., 2020. Evolution of the Global Carbon  
 603 Cycle and Climate Regulation on Earth. *Global Biogeochem. Cycles* 34,  
 604 e2018GB006061. <https://doi.org/https://doi.org/10.1029/2018GB006061>  
 605 James, R.H., Palmer, M.R., 2000. Marine geochemical cycles of the alkali elements and  
 606 boron: the role of sediments. *Geochim. Cosmochim. Acta* 64, 3111–3122.  
 607 [https://doi.org/https://doi.org/10.1016/S0016-7037\(00\)00418-X](https://doi.org/https://doi.org/10.1016/S0016-7037(00)00418-X)  
 608 Li, G., West, A.J., 2014. Evolution of Cenozoic seawater lithium isotopes: Coupling of  
 609 global denudation regime and shifting seawater sinks. *Earth Planet. Sci. Lett.* 401,  
 610 284–293.  
 611 Mackenzie, F.T., Garrels, R.M., 1966. Chemical mass balance between rivers and  
 612 oceans. *Am. J. Sci.* 264, 507–525.  
 613 McLennan, S.M., 1989. Rare earth elements in sedimentary rocks; influence of  
 614 provenance and sedimentary processes. *Rev. Mineral. Geochemistry* 21, 169–200.  
 615 Michalopoulos, P., Aller, R.C., 2004. Early diagenesis of biogenic silica in the Amazon  
 616 delta: alteration, authigenic clay formation, and storage. *Geochim. Cosmochim.*  
 617 *Acta* 68, 1061–1085.  
 618 Michalopoulos, P., Aller, R.C., 1995. Rapid Clay Mineral Formation in Amazon Delta  
 619 Sediments: Reverse Weathering and Oceanic Elemental Cycles. *Science* (80-. ).  
 620 270, 614–617.  
 621 Milliman, J.D., Farnsworth, K.L., 2013. River discharge to the coastal ocean: a global  
 622 synthesis. Cambridge University Press.  
 623 Misra, S., Froelich, P.N., 2012. Lithium Isotope History of Cenozoic Seawater:  
 624 Changes in Silicate Weathering and Reverse Weathering. *Science* (80-. ). 335,  
 625 818–823. <https://doi.org/10.1126/science.1214697>  
 626 Nägler, T.F., Schafer, H.-J., Gebauer, D., 1995. Evolution of the Western European

627 continental crust: implications from Nd and Pb isotopes in Iberian sediments.  
 628 Chem. Geol. 121, 345–357. <https://doi.org/https://doi.org/10.1016/0009->  
 629 2541(94)00129-V

630 Oelze, M., von Blanckenburg, F., Bouchez, J., Hoellen, D., Dietzel, M., 2015. The  
 631 effect of Al on Si isotope fractionation investigated by silica precipitation  
 632 experiments. Chem. Geol. <https://doi.org/http://dx.doi.org.insu.bib.cnrs.fr/10.1016/j.chemgeo.2015.01.002>

634 Pedregosa, F., Varoquaux, G., Gramfort, A., Michel, V., Thirion, B., Grisel, O., Blondel,  
 635 M., Prettenhofer, P., Weiss, R., Dubourg, V., Vanderplas, J., Passos, A.,  
 636 Cournapeau, D., Brucher, M., Perrot, M., Duchesnay, E., 2011. Scikit-learn:  
 637 Machine Learning in {P}ython. J. Mach. Learn. Res. 12, 2825–2830.

638 Pickering, K.T., Bayliss, N.J., 2009. Deconvolving tectono-climatic signals in deep-  
 639 marine siliciclastics, Eocene Ainsa basin, Spanish Pyrenees: Seesaw tectonics  
 640 versus eustasy. Geology 37, 203–206.

641 Pickering, K.T., Corregidor, J., 2005. Mass-Transport Complexes (MTCs) and  
 642 Tectonic Control on Basin-Floor Submarine Fans, Middle Eocene, South Spanish  
 643 Pyrenees. J. Sediment. Res. 75, 761–783. <https://doi.org/10.2110/jsr.2005.062>

644 Pistiner, J.S., Henderson, G.M., 2003. Lithium-isotope fractionation during continental  
 645 weathering processes. Earth Planet. Sci. Lett. 214, 327–339.

646 Pogge von Strandmann, P.A.E., James, R.H., van Calsteren, P., Gíslason, S.R., Burton,  
 647 K.W., 2008. Lithium, magnesium and uranium isotope behaviour in the estuarine  
 648 environment of basaltic islands. Earth Planet. Sci. Lett. 274, 462–471.

649 Qiu, L., Rudnick, R.L., McDonough, W.F., Merriman, R.J., 2009. Li and  $\delta^7\text{Li}$  in  
 650 mudrocks from the British Caledonides: metamorphism and source influences.  
 651 Geochim. Cosmochim. Acta 73, 7325–7340.

652 Rahman, S., Aller, R.C., Cochran, J.K., 2017. The Missing Silica Sink: Revisiting the  
 653 Marine Sedimentary Si Cycle Using Cosmogenic  $^{32}\text{Si}$ . *Global Biogeochem.*  
 654 *Cycles* 31, 1559–1578. <https://doi.org/10.1002/2017GB005746>  
 655 Rahman, S., Aller, R.C., Cochran, J.K., 2016. Cosmogenic  $^{32}\text{Si}$  as a tracer of biogenic  
 656 silica burial and diagenesis: Major deltaic sinks in the silica cycle. *Geophys. Res.*  
 657 *Lett.* 43, 7124–7132.  
 658 Santiago Ramos, D.P., Coogan, L.A., Murphy, J.G., Higgins, J.A., 2020. Low-  
 659 temperature oceanic crust alteration and the isotopic budgets of potassium and  
 660 magnesium in seawater. *Earth Planet. Sci. Lett.* 541, 116290.  
 661 [https://doi.org/https://doi.org/10.1016/j.epsl.2020.116290](https://doi.org/10.1016/j.epsl.2020.116290)  
 662 Savage, P.S., Georg, R.B., Williams, H.M., Halliday, A.N., 2013. The silicon isotope  
 663 composition of the upper continental crust. *Geochim. Cosmochim. Acta* 109, 384–  
 664 399. <https://doi.org/http://dx.doi.org/10.1016/j.gca.2013.02.004>  
 665 Shannon, R.D., 1976. Revised effective ionic radii and systematic studies of interatomic  
 666 distances in halides and chalcogenides. *Acta Crystallogr. Sect. A Cryst. physics,*  
 667 *diffraction, Theor. Gen. Crystallogr.* 32, 751–767.  
 668 <https://doi.org/10.1107/S0567739476001551>  
 669 Sholkovitz, E.R., 1976. Flocculation of dissolved organic and inorganic matter during  
 670 the mixing of river water and seawater. *Geochim. Cosmochim. Acta* 40, 831–845.  
 671 Sillen, L.G., 1967. The ocean as a chemical system. *Science* 156, 1189–1197.  
 672 <https://doi.org/10.1126/science.1189> [pii]  
 673 Teng, F.-Z., McDonough, W.F., Rudnick, R.L., Dalpé, C., Tomascak, P.B., Chappell,  
 674 B.W., Gao, S., 2004. Lithium isotopic composition and concentration of the upper  
 675 continental crust. *Geochim. Cosmochim. Acta* 68, 4167–4178.  
 676 Vigier, N., Decarreau, A., Millot, R., Carignan, J., Petit, S., France-Lanord, C., 2008.

Quantifying Li isotope fractionation during smectite formation and implications  
for the Li cycle. *Geochim. Cosmochim. Acta* 72, 780–792.

Wu, L., Percak-Dennett, E.M., Beard, B.L., Roden, E.E., Johnson, C.M., 2012. Stable  
iron isotope fractionation between aqueous Fe(II) and model Archean ocean Fe–  
Si coprecipitates and implications for iron isotope variations in the ancient rock  
record. *Geochim. Cosmochim. Acta* 84, 14–28.  
<https://doi.org/https://doi.org/10.1016/j.gca.2012.01.007>

Yang, C., Vigier, N., Yang, S., Revel, M., Bi, L., 2021. Clay Li and Nd isotopes  
response to hydroclimate changes in the Changjiang (Yangtze) basin over the past  
14,000 years. *Earth Planet. Sci. Lett.* 561, 116793.  
<https://doi.org/https://doi.org/10.1016/j.epsl.2021.116793>

Zhang, X. (Yvon), Saldi, G.D., Schott, J., Bouchez, J., Kuessner, M., Montouillout, V.,  
Henehan, M., Gaillardet, J., (Yvon) Zhang, X., Saldi, G.D., Schott, J., Bouchez, J.,  
Kuessner, M., Montouillout, V., Henehan, M., Gaillardet, J., 2021. Experimental  
constraints on Li isotope fractionation during the interaction between kaolinite and  
seawater. *Geochim. Cosmochim. Acta* 292, 333–347.  
<https://doi.org/https://doi.org/10.1016/j.gca.2020.09.029>

1 **Figure captions**

2 **Figure 1. Simplified (A) structural scheme of the southwestern Pyrenees Mountain**  
3 **range, (B) geological map of the Ainsa Basin, and (C) longitudinal profile across**  
4 **the palaeo-deltaic system of the Ainsa Basin (modified after Dreyer et al., (1999)).**  
5 **Ja: Jabierre de Olsón, Es: Escanilla, Me: Mesón de Ligüerre, and Co: Coscojuela**  
6 **sampling sites (see Fig. S1 for sedimentological sections).**

7 **Figure 2. “Box plots” of (A) major and (B) trace element concentrations**  
8 **normalized to Al for sediments from different depositional environments of the**  
9 **Ainsa Basin. Elements are ranked by increasing mean X/Al ratios from Mn to Ca**  
10 **and from Cs to Sr. Only a limited number of elements show enrichments in the**  
11 **seawater-contacted sediments compared to their terrestrial counterparts: Na and**  
12 **Fe for the major elements, and Li for trace elements.**

13 **Figure 3. Grain size (indexed by the Al/Si ratio) distribution of lithium (top),**  
14 **neodymium (middle), and silicon (bottom) isotope systems for bulk sediments of**  
15 **the alluvial plain, coastal plain, and marine (delta front and prodelta) depositional**  
16 **environments from the Ainsa Basin. Best-fit lines for relationships between isotope**  
17 **signatures (Li and Si) and grain size are shown as short dashed lines.**

18 **Figure 4. Relationship between  $\delta^7\text{Li}$  values and Li/Al ratios of the alluvial plain,**  
19 **coastal plain, and marine (delta front and prodelta) depositional environments**  
20 **from the Ainsa Basin. The grey bar shows the “baseline” formed by the**  
21 **composition of sediments without marine influence, and the arrows indicate the**  
22 **departure of sediments from this baseline towards Li enriched compositions and**  
23 **lower  $\delta^7\text{Li}$  values, due to authigenic clay formation in the marine realm. The**  
24 **estimated probability densities of Li/Al and  $\delta^7\text{Li}$  for each sediments group are**

respectively displayed at the top and the right of the figure. The most  $^6\text{Li}$ -enriched samples provide an upper boundary on the  $\delta^7\text{Li}$  of the authigenic component, which we estimate at -3‰.

**Figure 5. Relationships between  $\delta^7\text{Li}$  values and  $\text{Li}/(\text{Al}+\text{Fe})$ ,  $\text{Na}/(\text{Al}+\text{Fe})$  and  $\text{Li}/(\text{Al}+\text{Fe})$  ratios, and  $\delta^7\text{Li}$  values and  $\text{Li}/\text{Fe}$  ratio in sediments of the alluvial plain, coastal plain, and marine (delta front and prodelta) depositional environments from the Ainsa Basin. Best-fit lines are shown as short dashed lines. Colors for different samples are the same as in Fig. 1.**



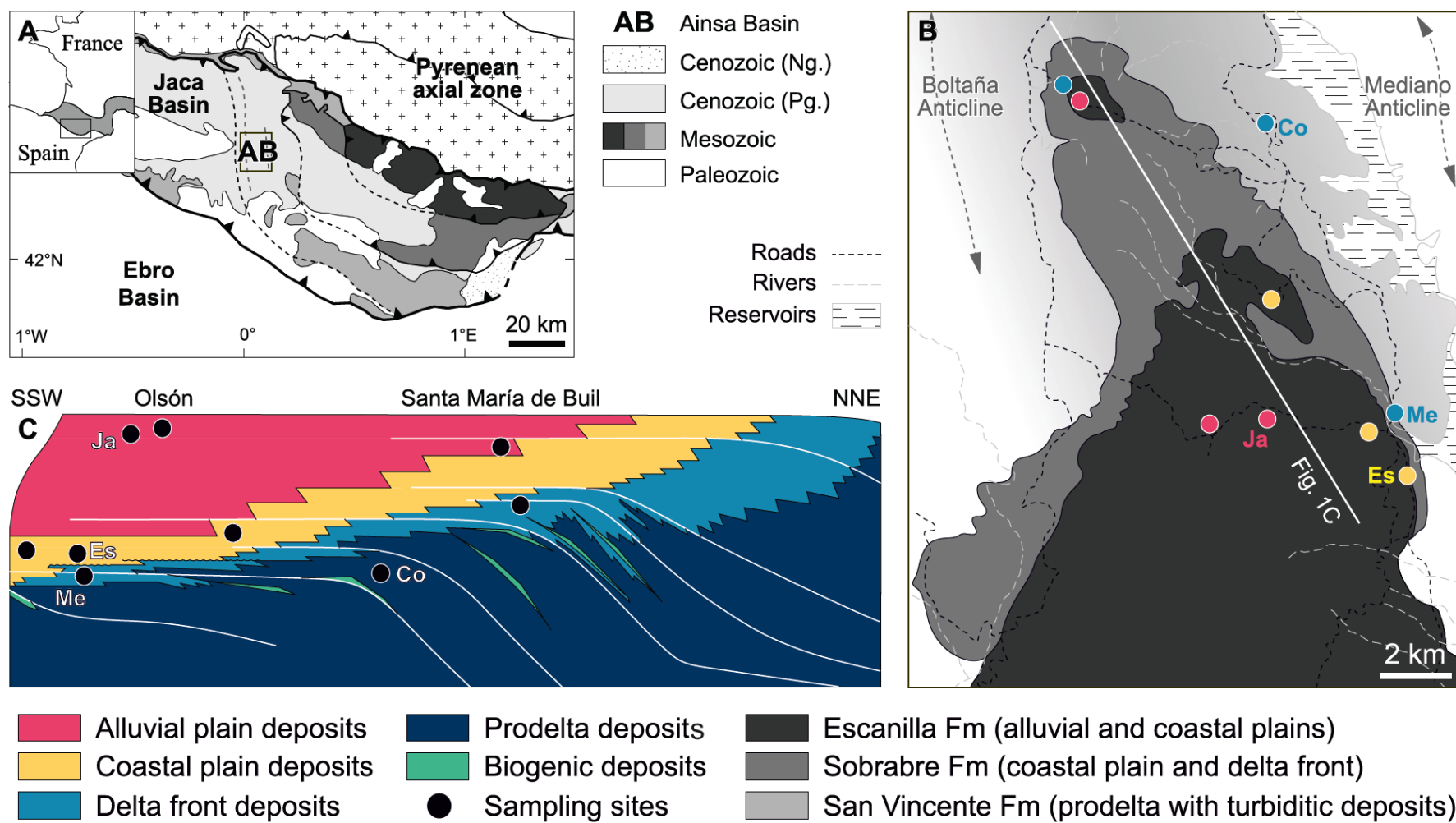


Figure 1

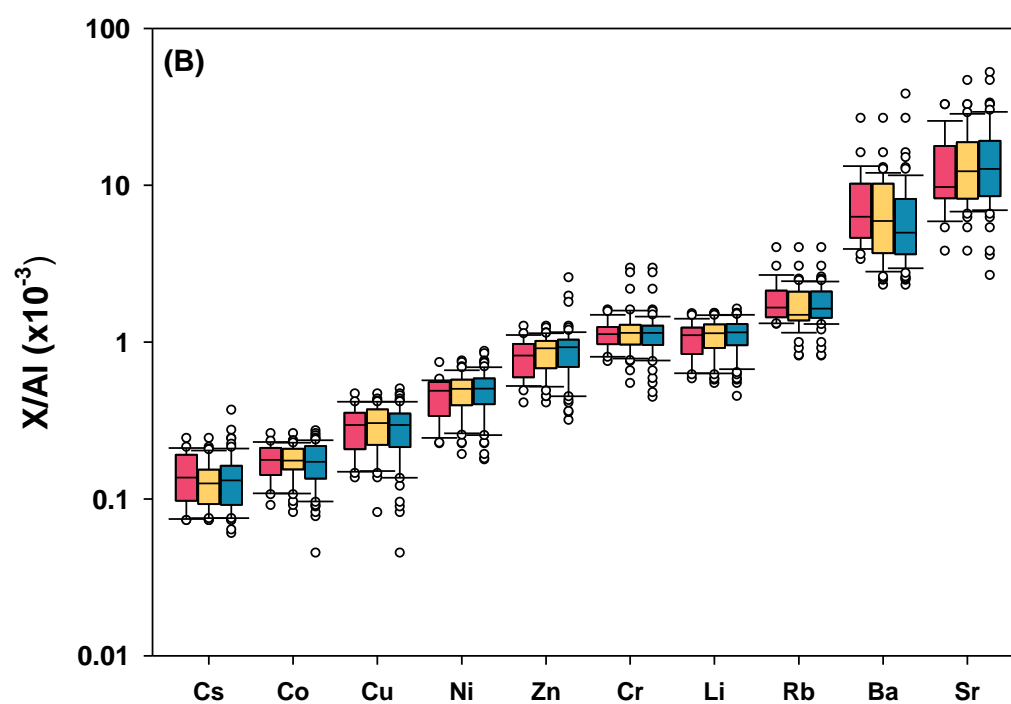
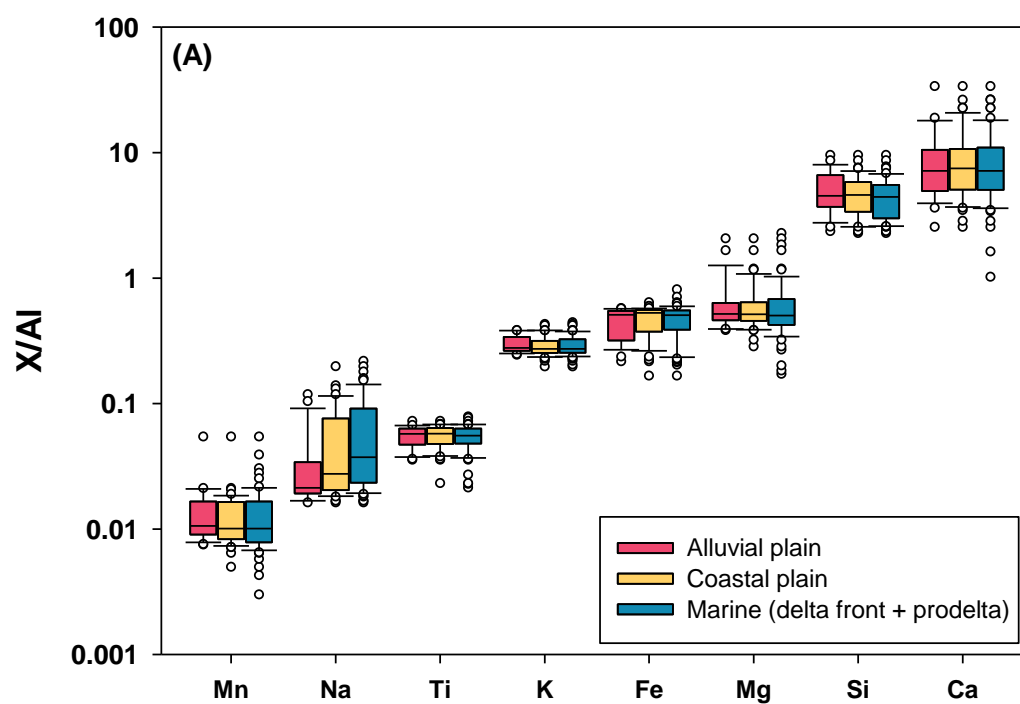


Figure 2

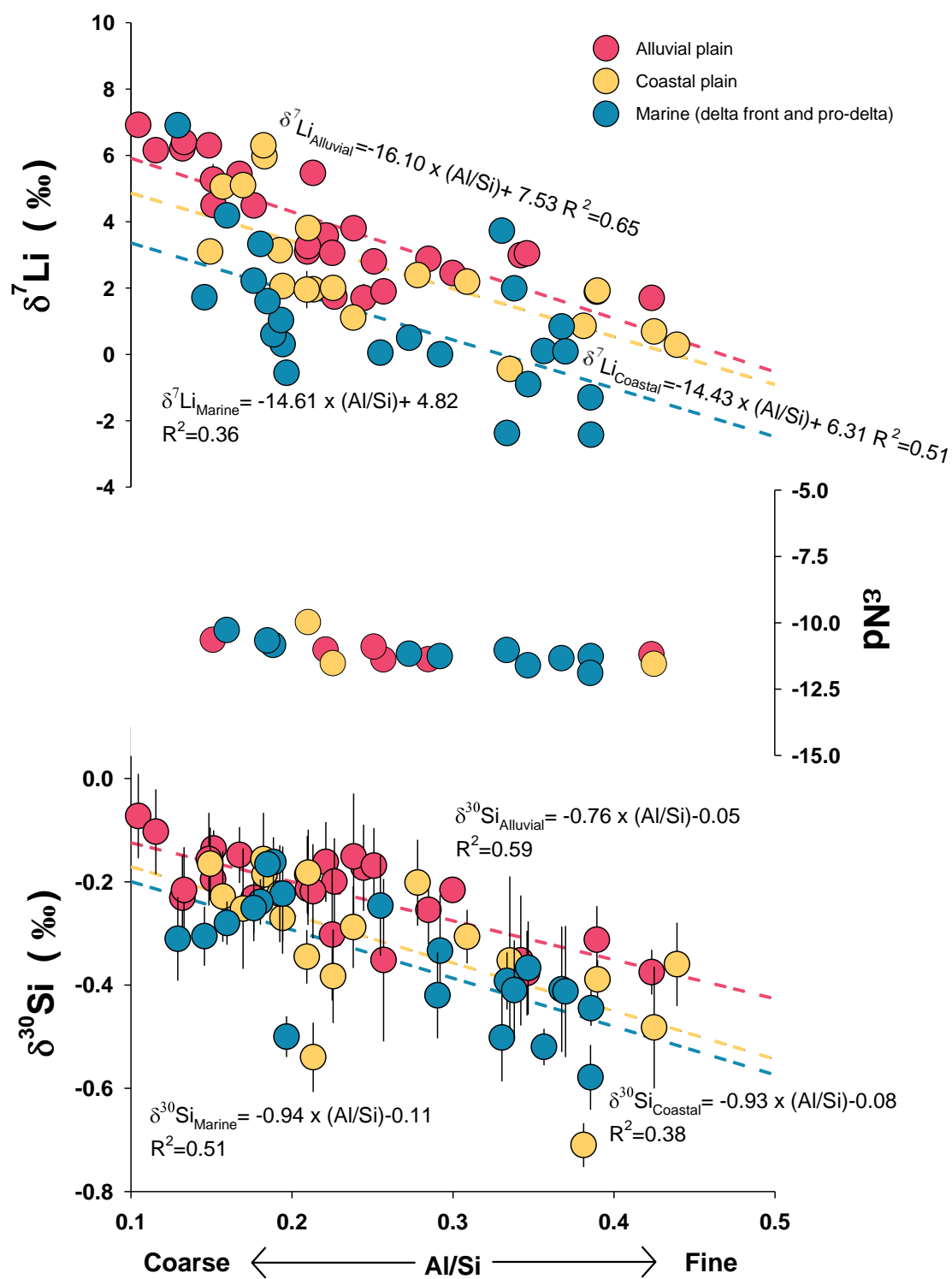


Figure 3

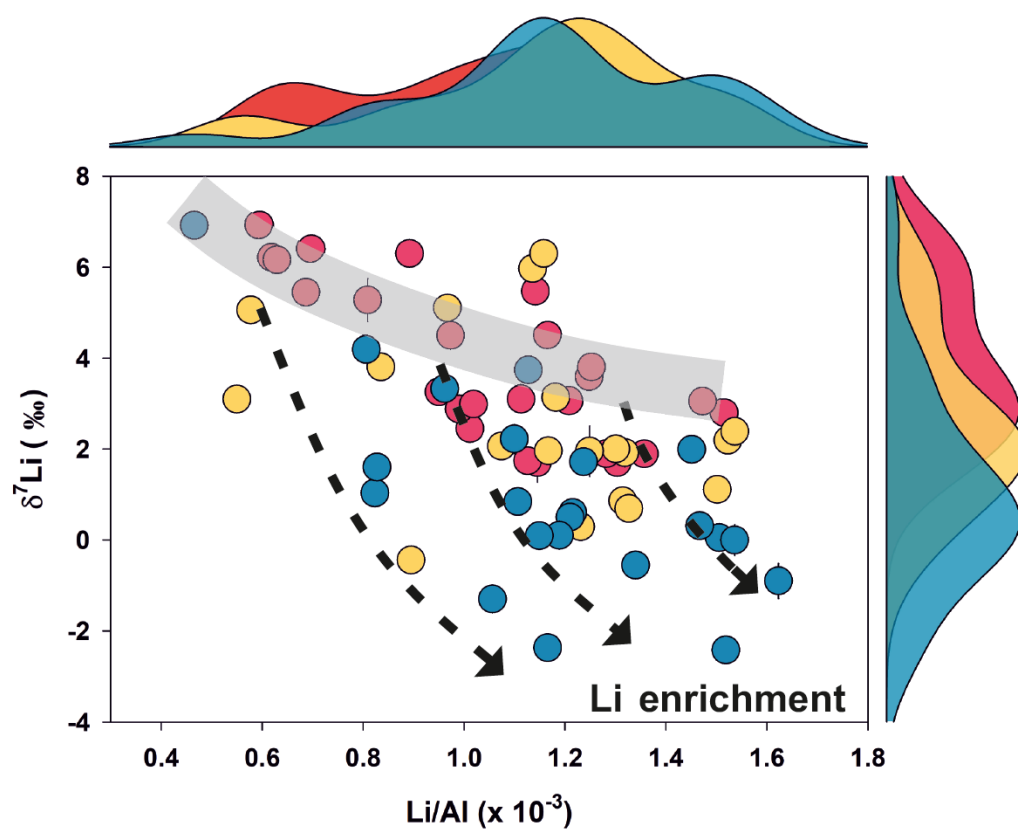


Figure 4

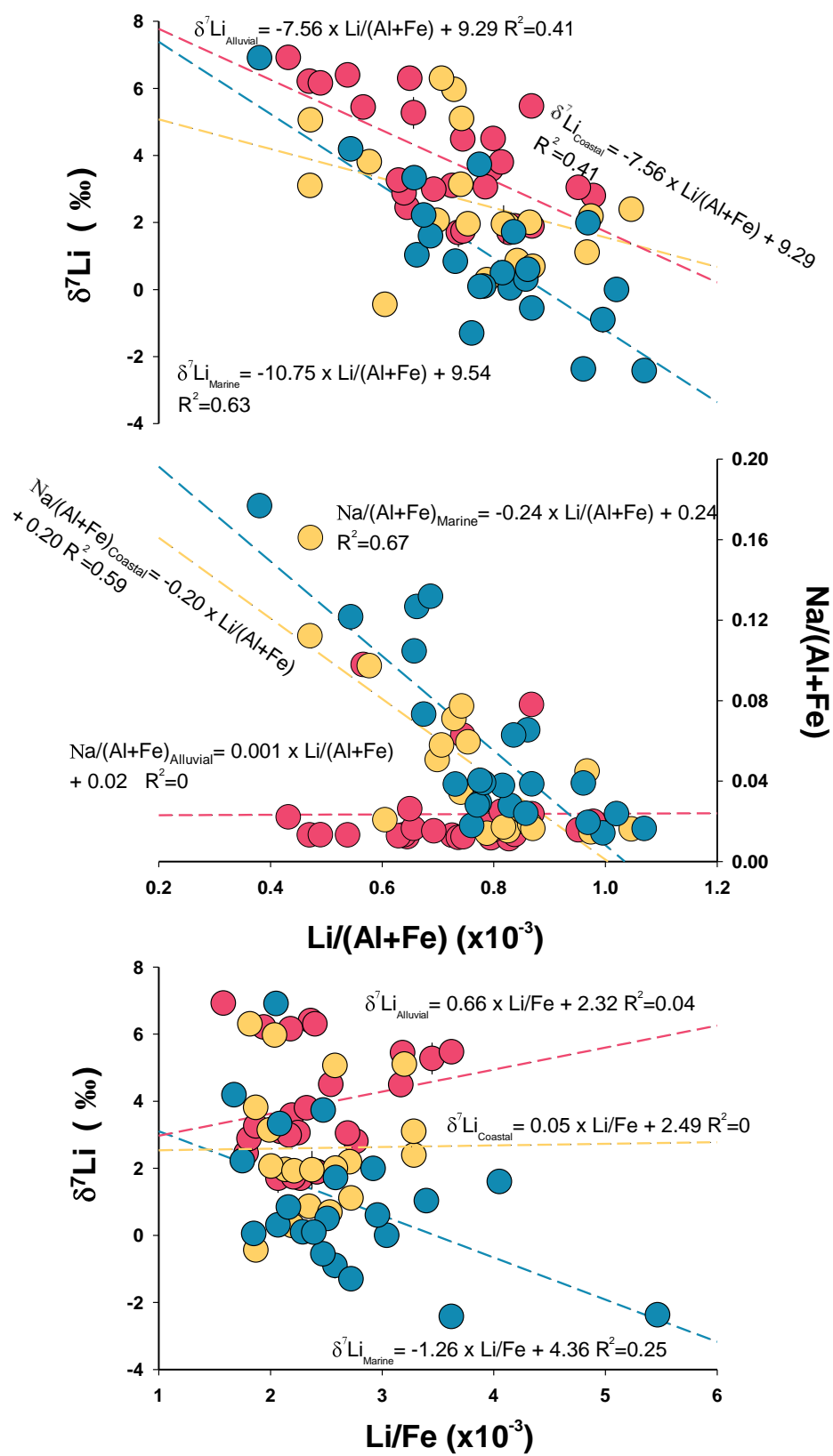


Figure 5

1    **Table captions**

2    **Table 1.** Summary of the thin section observations.

3    **Table 2.** Amount of Li extracted by the water rinsing experiments (in % of bulk  
4    content).

5    **Table 3.** Li isotope composition of the first and the last leach solution obtained from  
6    the HCl-leaching experiments.

7

8

9     **Supplementary tables**

10    **Table S1.** Locations, depositional environments,  $\delta^7\text{Li}$  and  $\delta^{30}\text{Si}$  values (in ‰),  $\epsilon\text{Nd}$ ,  
11    and Al/Si ratios of the samples collected in the Ainsa Basin.

12    **Table S2.** Major element concentrations (expressed in weight percent oxides) of the  
13    samples collected in the Ainsa Basin.

14  
15    **Table S3.** Trace elements concentrations (in ppm) of the samples collected in the Ainsa  
16    Basin.

17  
18    **Table S4.** HCl extracted cations (Ca, Li, Al, and Fe) in proportion to bulk sample (%).

19  
20    **Table S5.** Average alkali elements concentration (normalized to Al) in sediments  
21    deposited in different environments.

22  
23

**Table 1.** Summary of the thin section observations.

<i><b>Depositional environment</b></i>	<i><b>Coarse fraction</b></i>	<i><b>Fine fraction</b></i>
<b>Alluvial</b>	Coarse- to medium-grained sandstones mainly composed of angular to subangular detrital quartz and carbonates (crystalline, bioclastic, and micritic limestones), together with common detrital oxides or hydroxides and a few unweathered grains of detrital feldspars, micas, pyroxene, amphiboles, sandstones, and siltstones, surrounded by a calcite cement  <i>Example: sample SA 13 (Fig. S2A)</i>	Medium-grained sandstones to siltstones mainly composed of subangular detrital quartz and carbonates (crystalline and micritic limestones), together with common detrital oxides or hydroxides and a few unweathered grains of detrital feldspars, micas, pyroxene, amphiboles, and siltstones, surrounded by a clay matrix and/or a calcite cement  <i>Example: sample SA 15 (Fig. S2B)</i>
<b>Coastal</b>	Coarse- to medium-grained sandstones mainly composed of angular to subangular detrital quartz and carbonates (crystalline, bioclastic, and micritic limestones), together with common detrital oxides or hydroxides and a few unweathered grains of detrital feldspars, micas, pyroxene, amphiboles, sandstones, and siltstones, surrounded by a calcite cement  <i>Example: sample SC 6 (Fig. S2C)</i>	Medium-grained sandstones to siltstones mainly composed of subangular detrital quartz and carbonates (crystalline and micritic limestones), together with common detrital oxides or hydroxides and a few unweathered grains of detrital feldspars, micas, pyroxene, amphiboles, and siltstones, surrounded by a clay matrix and/or a calcite cement  <i>Example: sample SC 8 (Fig. S2D)</i>
<b>Marine</b>	Coarse- to medium-grained sandstones mainly composed of angular to subangular detrital quartz and carbonates (crystalline, bioclastic, and micritic limestones), together with bioclasts (benthic foraminiferas and echinoderm remains) and a few unweathered grains of detrital feldspars, micas, pyroxene, amphiboles, sandstones, siltstones, and oxides or hydroxides, surrounded by a calcite cement  <i>Example: sample SD 23 (Fig. S2E)</i>	Coarse- to medium-grained sandstones mainly composed of subangular detrital quartz and carbonates (crystalline, bioclastic, and micritic limestones), together with bioclasts (benthic foraminiferas and echinoderm remains) and a few unweathered grains of detrital feldspars, micas, pyroxene, amphiboles, siltstones, and oxides or hydroxides, surrounded by a clay and/or micrite matrix  <i>Example: sample ST 5 (Fig. S2F)</i>



28 **Table 2.** Amount of Li extracted by the water rinsing experiments (in % of bulk content).

29

Sample name	1 <sup>st</sup> rinse	2 <sup>nd</sup> rinse	3 <sup>rd</sup> rinse	Total rinsed Li	$\delta^7\text{Li}$	2 s.d.
Alluvial sediments						
SA3	0.10%	0.04%	0.03%	0.17%		
SA4	0.17%	0.06%	0.04%	0.28%		
SA6	0.23%	0.10%	0.10%	0.43%		
SA9	0.13%	0.05%	0.05%	0.23%		
SA11	0.16%	0.06%	0.05%	0.27%		
SA15	0.11%	0.05%	0.04%	0.20%		
SA22	0.12%	0.06%	0.04%	0.22%		
Seawater contacted sediments (coastal and marine)						
SC4	0.24%	0.07%	0.04%	0.35%	10.57	0.02
SC11	0.09%	0.04%	0.02%	0.15%	12.34	0.10
SC21	0.15%	0.04%	0.03%	0.22%	12.84	0.13
SD3	0.68%	0.12%	0.07%	0.87%	2.15	0.07
SD7	0.39%	0.08%	0.05%	0.52%	1.91	0.17
SD21	0.23%	0.06%	0.03%	0.32%	2.71	0.11
SD23	0.33%	0.10%	0.05%	0.48%	7.50	0.13
ST5	0.29%	0.17%	0.11%	0.57%	12.14	0.21

30

**Table 3.** Li isotope composition of the first and the last leach solution obtained from the HCl-leaching experiments.

Sample	First leach			Third leach		
	$\delta^7\text{Li}$	Al/Ca	Fe/Ca	$\delta^7\text{Li}$	Al/Ca	Fe/Ca
Alluvial sediments						
SA 4	3.68±0.24	3.91×10 <sup>-6</sup>	6.97×10 <sup>-5</sup>	-1.73 ± 0.20	9.67×10 <sup>-2</sup>	5.08×10 <sup>-2</sup>
SA 9	5.52±0.13	1.61×10 <sup>-5</sup>	8.43×10 <sup>-5</sup>	-2.28 ± 0.21	3.94×10 <sup>-2</sup>	4.30×10 <sup>-2</sup>
SA 11	2.60±0.07	5.29×10 <sup>-6</sup>	6.67×10 <sup>-5</sup>	0.13 ± 0.24	2.85×10 <sup>-2</sup>	2.27×10 <sup>-2</sup>
SA 15	4.61±0.10	7.30×10 <sup>-6</sup>	6.93×10 <sup>-5</sup>	-0.45 ± 0.26	3.45×10 <sup>-2</sup>	2.56×10 <sup>-2</sup>
Seawater contacted sediments (coastal and marine)						
SD 3	-0.55±0.09	3.11×10 <sup>-5</sup>	7.51×10 <sup>-5</sup>	-6.01 ± 0.14	6.26×10 <sup>-2</sup>	1.00×10 <sup>-1</sup>
SD 7	-6.32±0.08	1.49×10 <sup>-2</sup>	2.72×10 <sup>-2</sup>	-3.53 ± 0.27	3.10×10 <sup>-1</sup>	3.94×10 <sup>-1</sup>
ST 5	2.88±0.22	2.29×10 <sup>-5</sup>	8.51×10 <sup>-5</sup>	-4.67 ± 0.37	7.80×10 <sup>-2</sup>	1.95×10 <sup>-1</sup>
SC 21	6.16±0.37	1.20×10 <sup>-5</sup>	6.60×10 <sup>-5</sup>	-2.83 ± 0.30	3.43×10 <sup>-2</sup>	2.38×10 <sup>-2</sup>

### **S1.1 Lithium isotope measurements**

A double-step separation protocol using cation exchange resin (Biorad, AG50W-X12, 200-400 mesh) was employed in order to separate Li from the sample matrix (Zhang et al., 2021). During each separation session, five reference materials (BHVO-2, JB-2, NASS-6, SRM-2709a, and TILL-1) were routinely processed together with samples to evaluate the quality of this protocol. The Li isotope composition of the purified samples was measured using a Thermo Fisher Neptune Plus MC-ICP-MS. The pure Li standard solutions IRMM-016 and SPEC were routinely used to monitor the instrumental stability, while the L-SVEC solution was used as a bracketing standard to correct for instrumental mass fractionation. Accurate and reproducible Li isotope compositions for IRMM-016 ( $\delta^7\text{Li}=0.13\pm0.17\text{‰}$ , 2 SD, n=36), SPEC ( $\delta^7\text{Li}=94.32\pm0.19\text{‰}$ , 2 SD, n=26), NASS-6 ( $\delta^7\text{Li}=30.95\pm0.51\text{‰}$ , 2 SD, n=12), BHVO-2 ( $\delta^7\text{Li}=4.66\pm0.78\text{‰}$ , 2 SD, n=11), SRM-2709a ( $\delta^7\text{Li}=-0.30\pm0.58\text{‰}$ , 2 SD, n=13), TILL-1 ( $\delta^7\text{Li}=6.69\pm0.68\text{‰}$ , 2 SD, n=14), and JB-2 ( $\delta^7\text{Li}=4.72\pm0.80\text{‰}$ , 2 SD, n=15) were obtained. All the results are in good agreement with values reported in previous studies (Brand et al., 2014; Dellinger et al., 2014; Weynell et al., 2017; Kuessner et al., 2020).

### **S1.2 Silicon isotope measurements**

In order to analyse the Si isotope composition, an aliquot of each crushed sample was first digested using an alkali (NaOH) fusion method (Georg et al., 2006), and the Si concentration of digested sample solution was analysed using ICP-Q-MS. Then, a widely-adopted Si separation protocol was used (Georg et al., 2006; Pringle et al., 2016) using AG50W-X12 (200-400 mesh) resin. Si isotope composition was measured on a Thermo Fisher Neptune Plus MC-ICP-MS within 24 hours after the Si separation. The well-characterized reference material BHVO-2 was routinely analysed as an external standard to check the quality of the separation protocol and of the isotope measurements. The reference material National

Bureau of Standards 28 Sand Quartz (NBS-28, or also called NIST RM-8546) was processed through the same digestion and separation methods and was used as the bracketing standard to correct for instrumental mass fractionation. The Si isotope composition is expressed in  $\delta$ -notation in the unit of ‰ related to NBS-28:  $\delta^x\text{Si} = [({}^x\text{Si}/{}^{28}\text{Si})_{\text{Sample}}/({}^x\text{Si}/{}^{28}\text{Si})_{\text{NBS-28}} - 1] \times 1000$ , where  $x=29$  or  $30$ . Mass-dependent fractionation of Si isotopes across all samples is indicated by the linear relationship observed between  $\delta^{30}\text{Si}$  and  $\delta^{29}\text{Si}$  across all samples, with a slope value of 0.5153, which is between the value of kinetic fractionation (0.5092; Young et al., 2002) and that of equilibrium fractionation (0.5178; Young et al., 2002), undistinguishable from the two fractionations. The  $\delta^{30}\text{Si}$  value of BHVO-2 measured in this study ( $-0.29 \pm 0.05\text{‰}$ , 2 SD,  $n=21$ ) is in agreement with previously reported values (Zambardi and Poitrasson, 2011; Savage et al., 2013).

### **S1.3 Neodymium isotope measurements**

To separate Nd from the matrix, we have employed a double-column method (Caro et al., 2006). Sample solution was first allowed to pass a column packed with the TRU-spec resin (Eichrom) to separate rare earth elements from the sample matrix, then to pass a second column packed with the Ln-spec resin (Eichrom) to further purify Nd. Finally, Nd isotope composition was measured on a Neptune MC-ICP-MS, using a  ${}^{142}\text{Nd}/{}^{144}\text{Nd}$  ratio of 0.7218 for internal correction of instrumental mass fractionation. In this study, the Nd isotope composition is expressed in  $\epsilon$ -notation:  $\epsilon\text{Nd} = [({}^{143}\text{Nd}/{}^{144}\text{Nd})_{\text{Sample}}/({}^{143}\text{Nd}/{}^{144}\text{Nd})_{\text{CHUR}} - 1] \times 10000$  where CHUR stands for chondritic uniform reservoir ( ${}^{143}\text{Nd}/{}^{144}\text{Nd} = 0.512638$ ). The reported results are within an analytical uncertainty estimated at  $\sim 0.2$   $\epsilon\text{Nd}$  units from repeated runs of standard solutions.

- Brand, W.A., Coplen, T.B., Vogl, J., Rosner, M., and Prohaska, T., 2014, Assessment of international reference materials for isotope-ratio analysis (IUPAC Technical Report): Pure and Applied Chemistry, v. 86, p. 425–467.
- Caro, G., Bourdon, B., Birck, J.-L., and Moorbath, S., 2006, High-precision  $^{142}\text{Nd}/^{144}\text{Nd}$  measurements in terrestrial rocks: constraints on the early differentiation of the Earth's mantle: *Geochimica et Cosmochimica Acta*, v. 70, p. 164–191.
- Dellinger, M., Gaillardet, J., Bouchez, J., Calmels, D., Galy, V., Hilton, R.G., Louvat, P., and France-Lanord, C., 2014, Lithium isotopes in large rivers reveal the cannibalistic nature of modern continental weathering and erosion: *Earth and Planetary Science Letters*, v. 401, p. 359–372, doi:<http://dx.doi.org/10.1016/j.epsl.2014.05.061>.
- Georg, R.B., Reynolds, B.C., Frank, M., and Halliday, A.N., 2006, New sample preparation techniques for the determination of Si isotopic compositions using MC-ICPMS: *Chemical Geology*, v. 235, p. 95–104, doi:<http://dx.doi.org/insu.bib.cnrs.fr/10.1016/j.epsl.2006.07.006>.
- Kuessner, M.L., Gourgiotis, A., Manhès, G., Bouchez, J., Zhang, X., and Gaillardet, J., 2020, Automated Analyte separation by Ion Chromatography using a Cobot Applied to Geological Reference Materials for Li Isotope Composition: *Geostandards and Geoanalytical Research*, doi:10.1111/ggr.12295.
- Pringle, E.A., Moynier, F., Savage, P.S., Jackson, M.G., Moreira, M., and Day, J.M.D., 2016, Silicon isotopes reveal recycled altered oceanic crust in the mantle sources of Ocean Island Basalts: *Geochimica et Cosmochimica Acta*, v. 189, p. 282–295, doi:<http://dx.doi.org/insu.bib.cnrs.fr/10.1016/j.gca.2016.06.008>.
- Savage, P.S., Georg, R.B., Williams, H.M., and Halliday, A.N., 2013, The silicon isotope composition of the upper continental crust: *Geochimica et Cosmochimica Acta*, v. 109, p. 384–399, doi:<http://dx.doi.org/10.1016/j.gca.2013.02.004>.

- Weynell, M., Wiechert, U., and Schuessler, J.A., 2017, Lithium isotopes and implications on chemical weathering in the catchment of Lake Donggi Cona, northeastern Tibetan Plateau: *Geochimica et Cosmochimica Acta*, v. 213, p. 155–177, doi:<https://doi.org/10.1016/j.gca.2017.06.026>.
- Young, E.D., Galy, A., and Nagahara, H., 2002, Kinetic and equilibrium mass-dependent isotope fractionation laws in nature and their geochemical and cosmochemical significance: *Geochimica et Cosmochimica Acta*, v. 66, p. 1095–1104.
- Zambardi, T., and Poitrasson, F., 2011, Precise Determination of Silicon Isotopes in Silicate Rock Reference Materials by MC-ICP-MS: *Geostandards and Geoanalytical Research*, v. 35, p. 89–99.
- Zhang, X. (Yvon) et al., 2021, Experimental constraints on Li isotope fractionation during the interaction between kaolinite and seawater: *Geochimica et Cosmochimica Acta*, v. 292, p. 333–347, doi:<https://doi.org/10.1016/j.gca.2020.09.029>.

## **Supplementary figures**

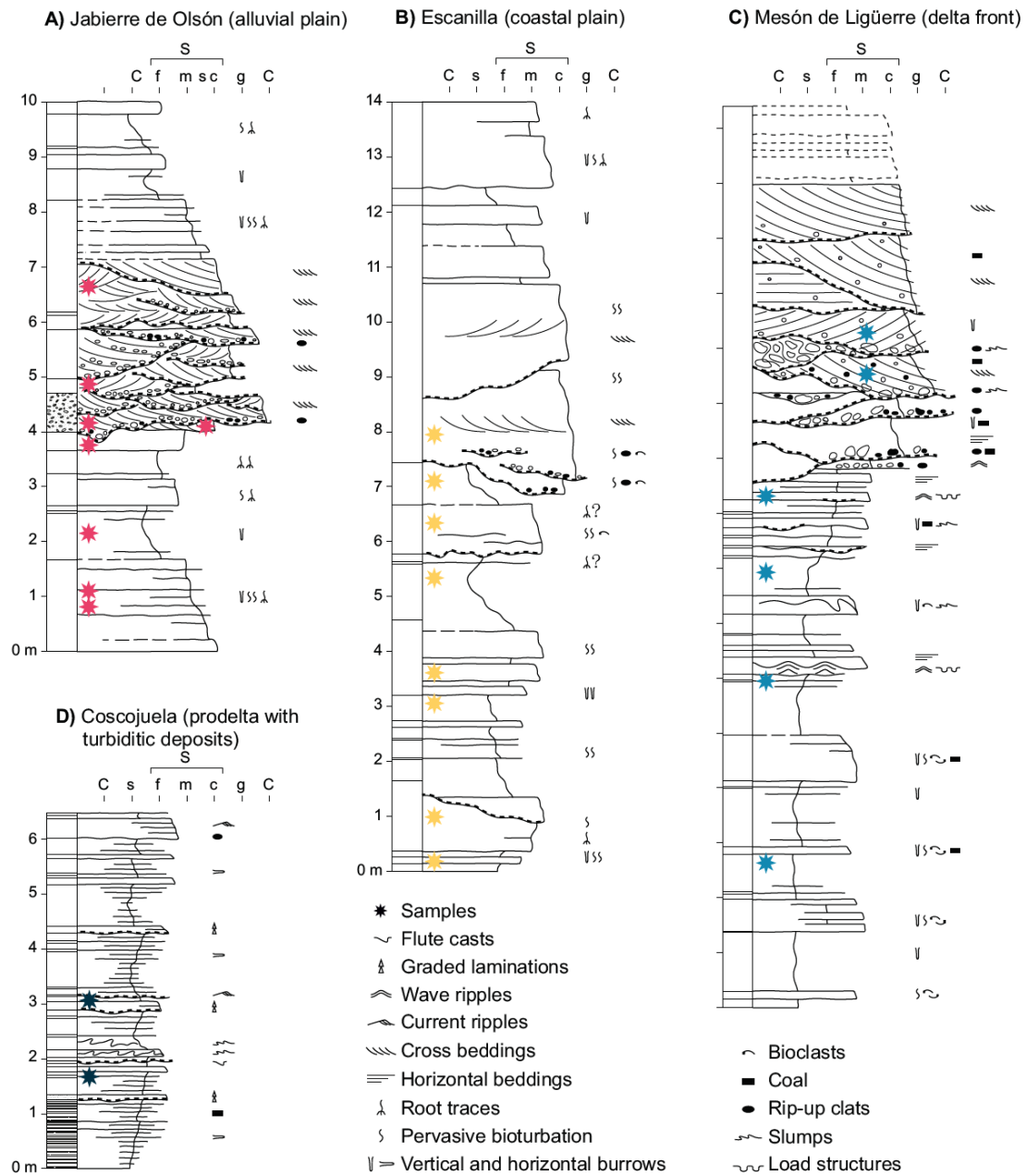
**Figure S1. Examples of sedimentological sections representative of deposits from the different environments sampled through the deltaic complex in the Ainsa Basin.**

**Figure. S2 Pictures of thin sections representative of deposits from the different environments sampled through the deltaic complex in the Ainsa Basin. These pictures were taken with an optical microscope using plane-polarized light above and cross-polarized light below.**

**Figure S3. Relationship between Li concentration and the total contents of Al and Fe.**

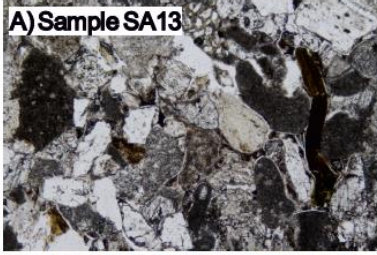
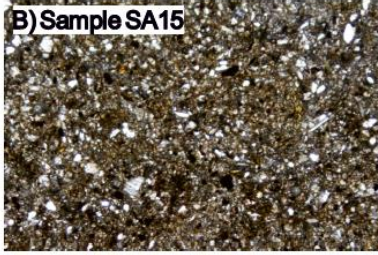
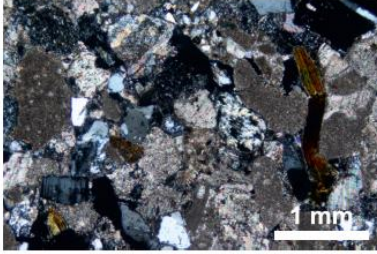
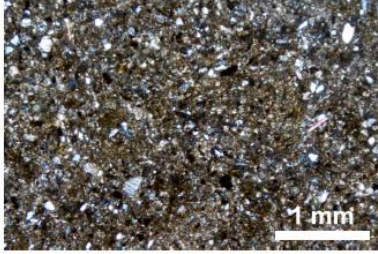
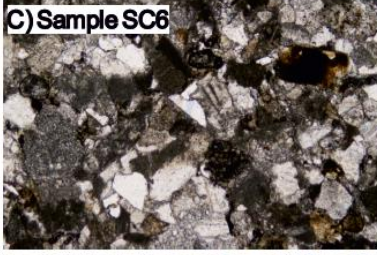
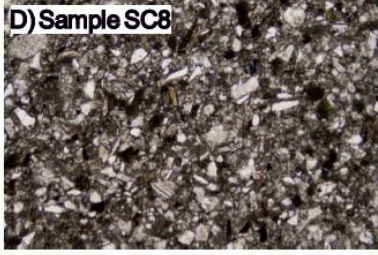
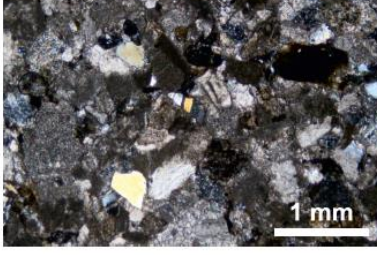
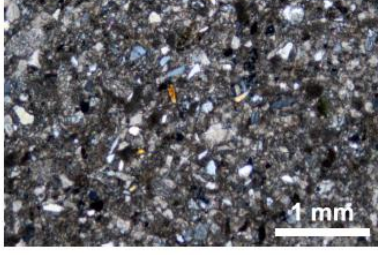
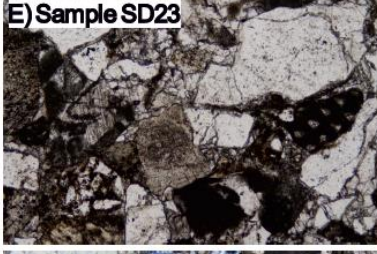
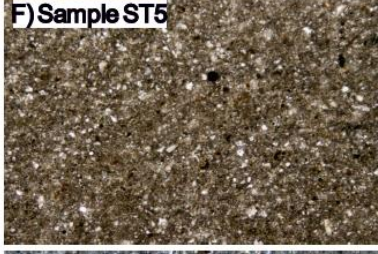
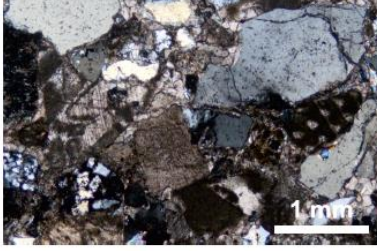
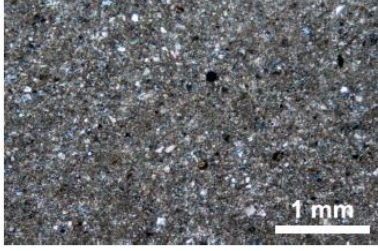
**Figure S4. Concentrations of Ca, Li, Al, and Fe in solutions from sequential HCl-leaching experiment performed on alluvial (displayed in red) and seawater-contacted (displayed in blue) sediments from the Ainsa Basin.**

**Figure S5.  $\delta^7\text{Li}$  values of the bulk samples and the solutions from the first (carbonate-bound Li) and third (Al–Fe associated Li) steps of the HCl-leaching experiments. The color code for alluvial, marine, and coastal samples the same as in Figure S3.**



**Figure S1**



<i>Depositional environment</i>	<i>Coarse fraction</i>	<i>Fine fraction</i>
<b>Alluvial</b>	A) Sample SA13 	B) Sample SA15 
		
<b>Coastal</b>	C) Sample SC6 	D) Sample SC8 
		
<b>Marine</b>	E) Sample SD23 	F) Sample ST5 
		

**Figure S2**

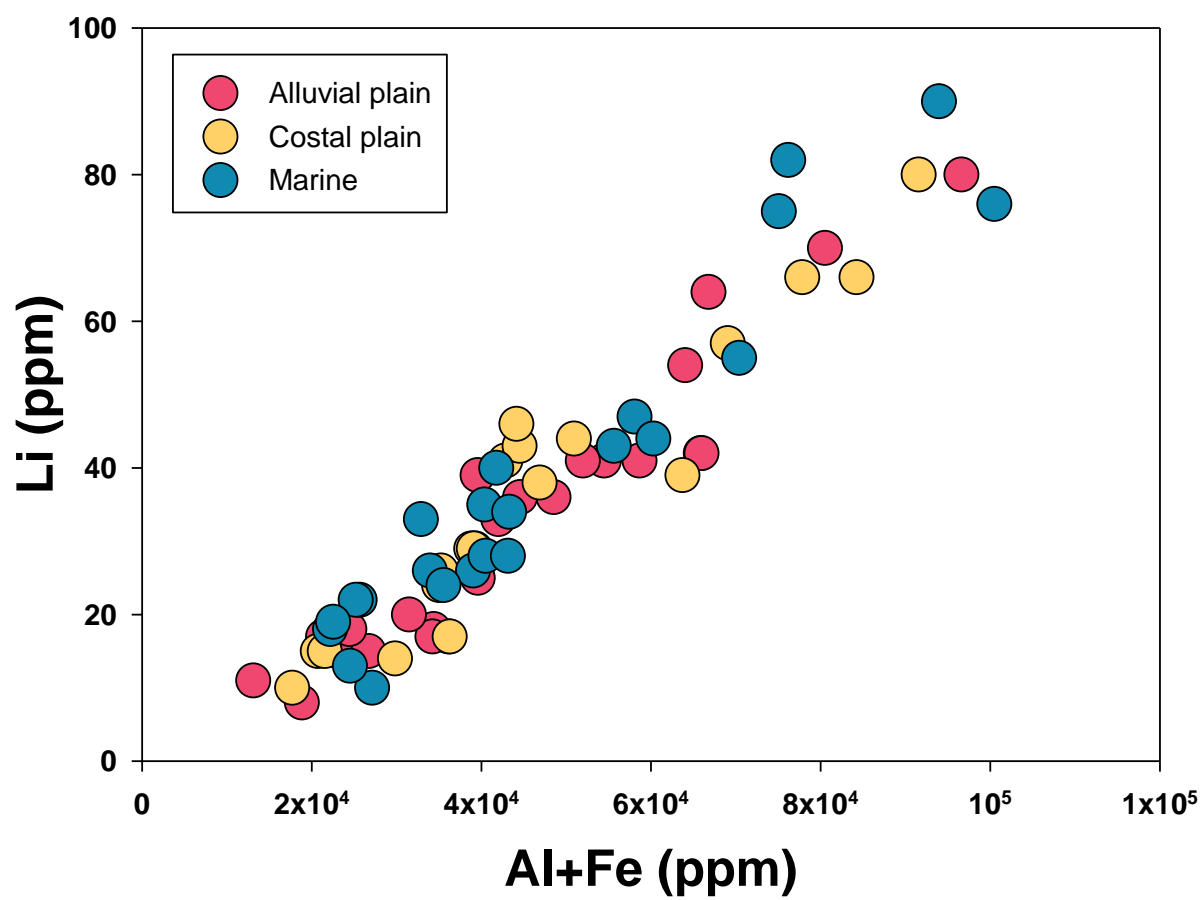


Figure. S3

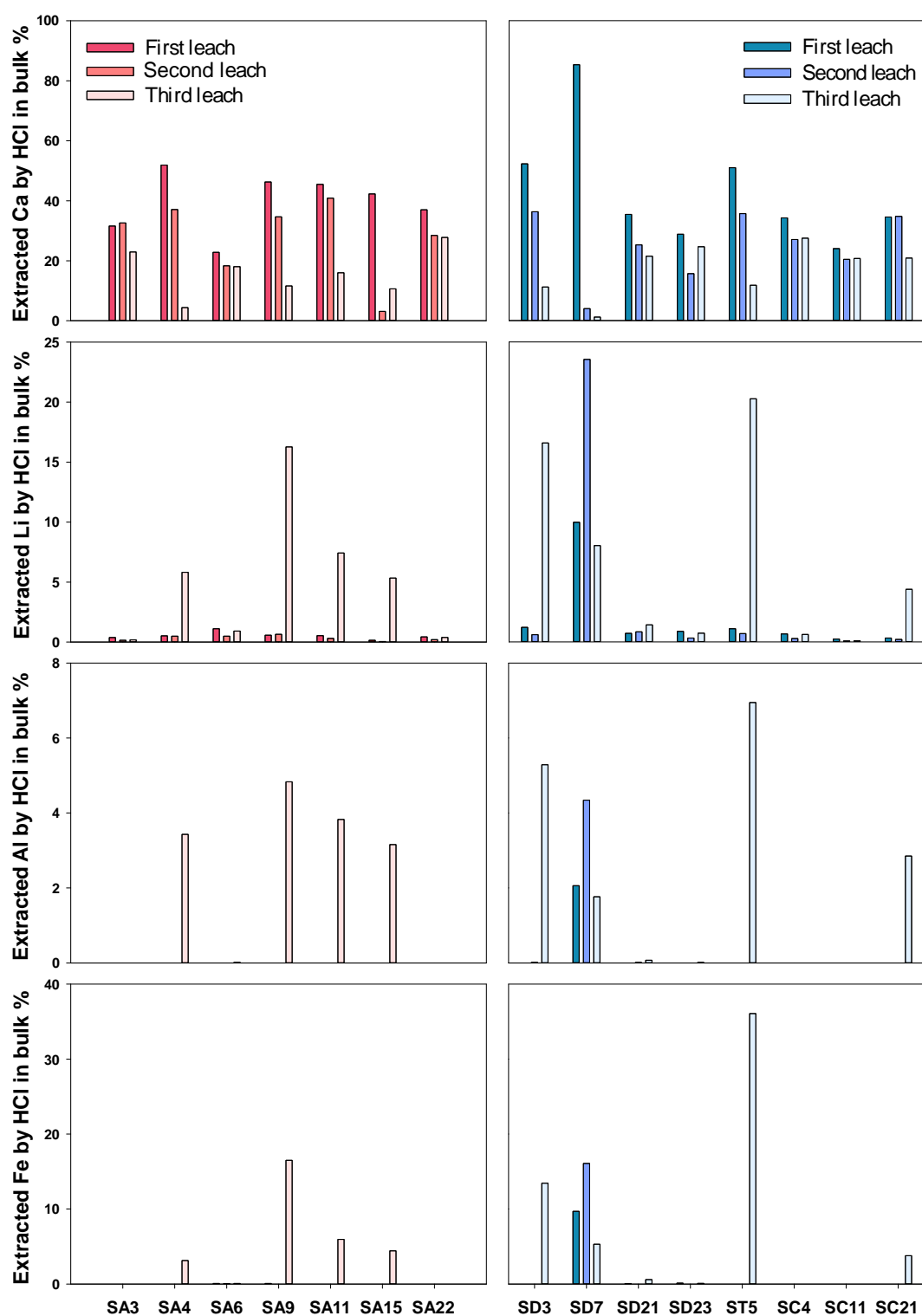


Figure S4

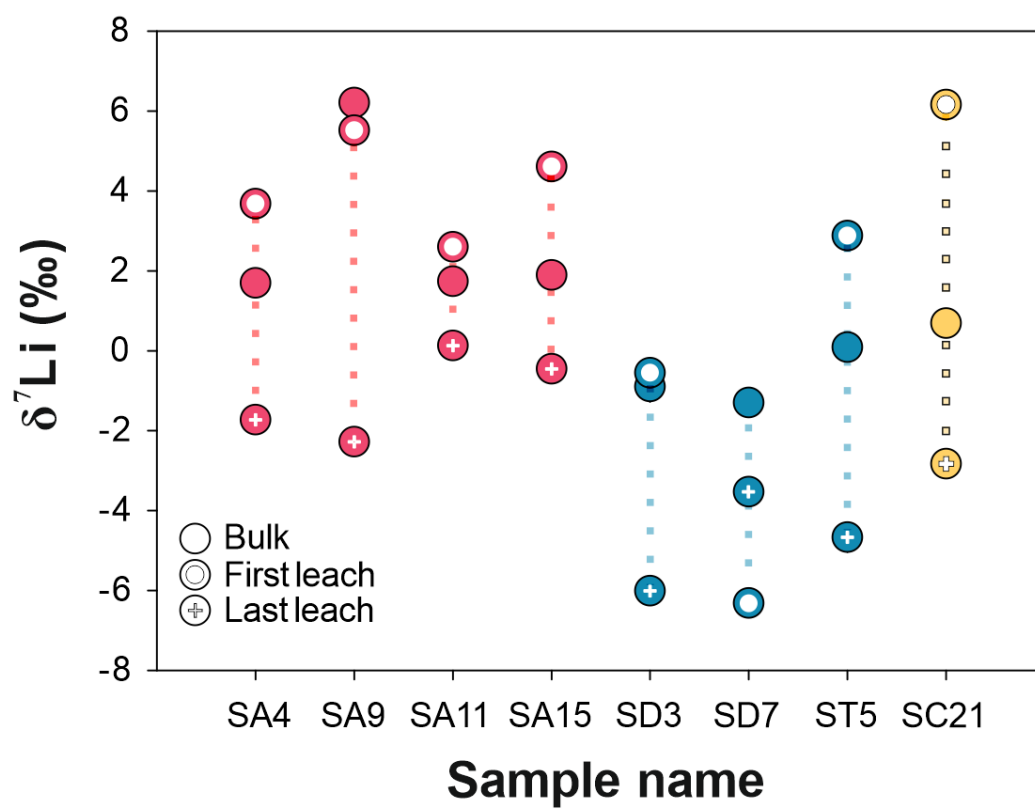


Figure S5